Frontiers in Bioscience Elite

Front. Biosci. (Elite Ed) **2025**; 17(4): 44344
https://doi.org/10.31083/FBE44344

Original Research

Targeting the *LRRK2 G2019S* Mutation Found in Parkinson's Disease: Efficiency of Biosynthesized Solid Lipid Nanoparticles for Therapeutic siRNA-Mediated Gene Therapy

Keelan Jagaran[1], Moganavelli Singh[1,*]

[1]Nano-Gene and Drug Delivery Laboratory, Discipline of Biochemistry, University of KwaZulu-Natal, 4000 Durban, South Africa
*Correspondence: singhm1@ukzn.ac.za (Moganavelli Singh)
Academic Editor: Hongwei Yao
Submitted: 28 June 2025 Revised: 25 July 2025 Accepted: 7 August 2025 Published: 18 December 2025

Abstract

Background: Parkinson's disease (PD) is a progressive neurodegenerative disorder with which the *leucine-Rich repeat kinase 2 glycine 2019 serine* (*LRRK2* G2019S) mutation is strongly associated. This mutation elevates kinase activity, disrupts mitochondrial function, increases reactive oxygen species (ROS) production, and impairs DNA repair mechanisms, all of which contribute to the pathogenesis of PD. Thus, addressing these pathological features through targeted delivery systems holds promise for more effective therapies. **Methods**: This study aimed to investigate the use of *Ginkgo biloba* leaf extract (EGB) to synthesize sphingomyelin-cholesterol solid lipid nanoparticles (SLNPs) functionalized with poly-L-lysine (EGB–PLL–SLNPs) for siRNA delivery targeting the *LRRK2 G2019S* mutation. SLNPs suspended in water (H_2O–PLL–SLNPs) served as the comparator. *In vitro* assays were conducted using either wild-type or *LRRK2 G2019S*-transformed SH-SY5Y and HEK293 cells. The 3-(4,5-dimethylthiazol-2-yl)-2,5-diphenyltetrazolium bromide (MTT) assay was employed to evaluate the cytotoxicity of the SLNPs and nanocomplexes; meanwhile, flow cytometry was used to assess caspase 3/7 activity, mitochondrial membrane potential, DNA damage, and ROS levels. **Results**: Treatment with EGB–PLL–SLNPs significantly improved mitochondrial health, reducing depolarized and dead cells and enhancing overall cell viability. ROS levels, DNA damage and kinase activity were significantly decreased compared to the control H_2O–PLL–SLNPs. **Conclusion**: The enhanced therapeutic outcomes observed with the EGB–PLL–SLNPs can be attributed to the bioactive compounds in EGB, particularly the flavonoids and terpenoids, such as quercetin and kaempferol. These molecules play crucial roles in stabilizing mitochondrial membranes, facilitating ATP synthesis, and regulating genes linked to mitochondrial biogenesis. The interaction between EGB and siRNA to mediate gene silencing provides a multifaceted approach to counteracting PD pathophysiology. This study demonstrates that EGB–PLL–SLNPs offer superior gene silencing and cytoprotective effects compared to conventional formulations. The integration of plant-based bioactives with nanomedicine enhances therapeutic delivery and efficacy, positioning biosynthesized PLL–SLNPs as a promising strategy for treating Parkinson's disease.

Keywords: Parkinson's disease; gene therapy; siRNA; Ginkgo biloba; SLNPs; nanomedicine; *LRRK2 G2019S*

1. Introduction

Parkinson's disease (PD) is the second most common neurodegenerative disorder globally, with a prevalence of 0.2% [1]. PD is characterized by the progressive loss of dopaminergic neurons (mDAs) in the midbrain, particularly in the substantia nigra [2,3]. While most PD cases are sporadic, approximately 15% are inherited, with familial genetic studies identifying 20 genes implicated in PD, and genome-wide association studies (GWAS) presenting about 90 loci [4]. Among these, the *leucine-rich repeat serine/threonine-protein kinase 2* (*LRRK2*) gene is associated with both familial and sporadic cases, underscoring the role of *LRRK2* in neurodevelopmental disorders [5]. Moreover, *LRRK2* is essential during development and binds to the disheveled (DLV) family proteins, which are mediators in the Wnt signaling pathways, and are crucial in embryonic development [6].

Mutations in this binding domain, especially the autosomal dominant c.6055G>A mutation, which leads to the *LRRK2* G2019S substitution, represent the most common genetic risk factor for PD [7–9]. Meanwhile, the *LRRK2* G2019S substitution mutation results in a 2- to 3-fold increase in kinase activity, although the exact mechanism for this remains unclear. Evidence suggests that this increase is associated with regulating mitochondrial dynamics, chaperone-mediated autophagy, and vesicle trafficking [10–12]. Moreover, the elevated expression of oxidative stress-related genes in G2019S-induced pluripotent stem cells further underscores the role of this mutation [13], while highlighting the pivotal role of these processes in PD pathogenesis.

Current therapeutics, such as LRRK2 inhibitors, have demonstrated protective efficacy but face challenges and adverse effects, including pulmonary fibrosis, and exhibit varying efficacy among patients, necessitating the development of a personalized therapeutic approach [14]. These

therapeutics struggle to effectively cross the blood–brain barrier (BBB), reducing their therapeutic efficacy [15]. The BBB is crucial for maintaining brain homeostasis by preventing circulating pathogens and toxins from entering the brain [16]. Recent advancements in alternative strategies to mitigate this barrier include the use of lipid nanoparticles (LNPs), specifically solid LNPs (SLNPs).

SLNPs have a size range of 40 to 1000 nm, enhanced bioavailability, controlled cargo release, a higher loading capacity, and the absence of organic solvents in the synthesis process, as well as cost-effective large-scale production [17]. These nanoparticles (NPs) utilize clathrin-mediated endocytosis to penetrate the BBB [18]. LNPs can be engineered to optimize performance for various diseases, with sphingomyelin (SM) and cholesterol (Chol) showing significant potential in treating PD. These lipid components enhance the efficacy of BBB crossing and contribute to membrane stability. SM plays a key role in maintaining myelin sheath integrity, facilitating nerve impulse transmission, and supporting BBB homeostasis through its involvement in lipid raft formation and signal transduction. Meanwhile, cholesterol improves nanoparticle stability, modulates pharmacokinetics, and prolongs circulatory half-life *in vivo* [19,20]. Together, the SM–Chol-derived SLNPs form nano-domains essential for synaptic plasticity and neurotransmitter release, offering a promising approach to PD treatment at a curative level.

The engineering of these SLNPs is crucial for promoting the desired functional outcomes. The biosynthesis of SLNPs with *Ginkgo biloba* leaf extracts (EGB) combines neuroprotective and antioxidant properties. SLNPs also act as a monoamine oxidase (MAO) inhibitor, preventing dopamine degradation. EGB extracts also increase muscular coordination, dopaminergic D2 receptor content, locomotor activity, and restore antioxidant enzymes in the striatum [21], providing a secondary therapeutic effect for PD treatment, albeit primarily palliative.

Thus, this study aimed to develop a novel biosynthesized SLNP delivery vehicle containing SM and Chol and functionalized with poly-L-lysine (PLL) for conjugation to the therapeutic siRNA. This SLNP–siRNA nanocomplex was formulated to target the *LRRK2* G2019S mutation in PD. The development of the nanocomplex also addresses the delivery challenges faced by naked siRNA, such as BBB crossing, nuclease degradation, and its polyanionic nature [14]. Additionally, this study examined PD at the basic genetic level and presents a promising dual therapeutic approach, advancing toward a curative treatment for PD.

2. Materials and Methods

2.1 Materials

Phosphate-buffered saline (PBS), 3-[4,5-dimethylthiazol-2-yl]-2,5-diphenyltetrazolium bromide (MTT), and dimethyl sulfoxide (DMSO) were purchased from Merck (Darmstadt, Germany). The luciferase and NanoBRET® TE intracellular kinase assay kits, as well as the *LRRK2*(G2019S)-NanoLuc® Fusion Vector, were obtained from Promega Corporation (Madison, WI, USA). The BLOCK-iT™ fluorescent control, Lipofectamine 2000, and the *LRRK2 (G2019S)* silencer RNA were sourced from Thermo Fisher Scientific Inc. (Waltham, MA, USA). The *LRRK2* (G2019S) Silencer® Select siRNA was purchased as a validated, pre-designed siRNA duplex that targets the *LRRK2* G2019S mutant allele (Thermo Fisher Scientific Inc., Waltham, MA, USA). The siRNA was chemically modified to enhance stability and reduce off-target effects; due to the proprietary nature of the siRNA, the exact sequence and modification details are not publicly disclosed by the manufacturer. The product is commercially available for the allele-specific silencing of *LRRK2* G2019S, and has been used in similar mutation-targeting studies. The Muse™ caspase-3/7, oxidative stress, multi-color DNA damage, and mitopotential kits were provided by Luminex (Austin, TX, USA). Sterile cell culture plasticware was procured from Nest Biotechnologies (Wuxi, Jiangsu, China). Trypsin-versene, Eagle's Minimum Essential Medium (EMEM), Dulbecco's modified Eagle medium/nutrient mixture F-12 (DMEM/F12), and antibiotic mixture (penicillin 5000 units/mL, streptomycin 5000 µg/mL) were supplied by Lonza BioWhittaker (Walkersville, MD, USA). Gamma-irradiated fetal bovine serum (FBS) was provided by Hyclone GE Healthcare (Logan, UT, USA). The embryonic kidney (HEK293) and neuroblastoma (SH-SY5Y) cells were originally sourced from the American Type Culture Collection (ATCC, Manassas, VA, USA), and authenticated by short tandem repeat (STR) profiling. Mycoplasma testing was performed on both cell lines as part of routine culture validation in our laboratory, as reported in a related study [22]. All reagents were of analytical grade, and 18 MΩ water (Milli-Q Academic, Millipore, Molsheim, France) was used in the preparations.

2.2 Synthesis of PLL-SC-SLNPs

The biologically synthesized PLL–SC–SLNPs, prepared using EGB as a reducing agent, were synthesized following the previously detailed protocols [22].

2.3 Characterization and Binding Studies

Characterization of the synthesized NPs was performed using ultraviolet (UV)-visible (UV-vis) and Fourier-transform infrared (FTIR) spectroscopy, transmission electron microscopy (TEM), and dynamic light scattering (DLS).

Binding studies were conducted using the ethidium bromide (EtBr) intercalation assay to measure binding and compaction of the NPs, the band shift assay to assess siRNA:NP complex formation, and the RNase protection assay to evaluate the stability of siRNA in the presence of

nuclease enzymes [23]. These techniques have been published previously [22].

2.4 Cell Culture and LRRK2 G2019S Transfection

All cell culture-based experiments were conducted in a class II biosafety laminar flow hood under sterile conditions. The embryonic kidney (HEK293) and neuroblastoma (SH-SY5Y) cells were propagated and maintained in 25 cm^2 tissue culture flasks containing 5 mL of complete medium (EMEM for HEK293 and DMEM/F12 for the SH-SY5Y cells), supplemented with 10% (v/v) FBS and 1% antibiotics (100 U/mL penicillin, 100 µg/mL streptomycin) in a HEPA class 100 Steri-Cult CO_2 incubator (Thermo Fisher Inc., Waltham, MA, USA). Cells were monitored daily under a Nikon TMS inverted microscope (Nikon Corp., Tokyo, Japan) and subcultured into multi-well plates for subsequent assays as needed.

The transformed cell lines were cultured similarly, with the LRRK2(G2019S)-NanoLuc® Fusion Vector introduced into the cells. Fusion complexes were prepared using 9.0 µg/mL of transfection carrier DNA and 1.0 µg/mL of the fusion vector in 1 mL of EMEM/DMEM/F12 assay medium (99% medium supplemented with 1% FBS). Lipofectamine 2000 (30 µL) was then added and mixed by inversion (5–10 times). The lipoplexes were incubated at ambient temperature for 20 minutes and then introduced into the cells at a ratio of 1:20 (complex). Following transfection and the appropriate growth periods described in the relevant sections, cells were subcultured into multi-well plates for each assay.

Although HEK293 cells are not of neuronal origin, these cells were included in this study as a comparative non-neuronal control cell line. Since *LRRK2* is a ubiquitously expressed gene and the G2019S mutation occurs in a germline autosomal-dominant manner, the pathological effects of this mutation are not restricted to neuronal tissue. Therefore, the inclusion of this cell line permitted the evaluation of mutation-driven cellular dysfunction. Furthermore, HEK293 cells exhibit stable growth and high transfection efficacy, thus providing a reliable baseline for interpreting the mutational-specific effects. This comparison enables a clear distinction between cell type-specific responses and mutation-dependent responses, thereby enhancing the overall interpretation of downstream therapeutic assays. Furthermore, HEK293 cells have been used as a standard cell line in numerous *in vitro* studies.

2.5 Cellular Uptake Studies

The cellular uptake assay, using a BLOCK-iT™ fluorescent oligo (Invitrogen catalog no. 13750062) for visualization, assessed the ability of the PLL–SLNPs to traverse the cellular membrane and localize in the nucleus. Wild-type and transformed cells were prepared and treated. Specifically, the transformed cells were trypsinized and seeded into clear 96-well plates at a density of 1.8×10^5 cells per well and incubated at 37 °C overnight. Nanocomplexes were prepared using the optimum binding ratios with 50 nM (0.067 µg) BLOCK-iT Oligo (1:1) and 100 nM BLOCK-iT Oligo (1:2) and incubated for 1 h. A positive control was performed using untreated cells to provide a comparative baseline. After incubation, the growth medium was replaced with fresh medium (EMEM + 10% FBS + 1% antibiotics), and the nanocomplexes were added to the cells, which were then incubated at 37 °C for 24 h. After removing the medium, the cells were washed with PBS (2×60 µL) and viewed under an Olympus CKX41 inverted phase contrast fluorescence microscope (Olympus Corporation, Tokyo, Japan) at an excitation wavelength of 494 nm and an emission wavelength of 519 nm.

Cells were then lysed with 80 µL reporter lysis buffer with gentle shaking on a STR 6 platform shaker (Stuart Scientific, Staffordshire, UK) at 30 rpm for 15 min. Subsequently, the cells were detached from the wells, and the cell lysates were transferred into a 96-well black plate. Fluorescence was measured using the Glomax Multi-Detection System (Promega Biosystems, Sunnyvale, CA, USA). Protein concentrations were determined using the standard bicinchoninic acid (BCA) assay. The fluorescence values were then normalized against the BCA assay results and expressed as relative fluorescent units (RFUs) per mg of protein.

2.6 The 3-(4,5-dimetylthiazol-2-yl)-2,5-diphenyltetrazolium Bromide (MTT) Assay

The cytotoxicity profiles of the transformed HEK293 and SH-SY5Y cells were reported in detail previously [22]. The cells were trypsinized and seeded into 96-well plates at a density of 1.8×10^5 cells per well and incubated at 37 °C overnight. Nanocomplexes were prepared in triplicate using the SLNP nanocomplexes at optimum binding ratios with 50 nM non-targeting siRNA (0.067 µg). The positive control, consisting of untreated cells, represented 100% survival. After incubation, the growth medium was replaced with fresh medium (EMEM + 10% FBS + 1% antibiotics). The nanocomplexes were added to the cells, and the cells were incubated at 37 °C for 48 h. The growth medium was then aspirated and replaced with 0.1 mL of EMEM (HEK 293) or DMEM/F12 (SH-SY5Y) medium containing 0.01 mL of MTT solution (5 mg/mL in PBS). After a further incubation at 37 °C for 4 h, the MTT-infused medium was removed, and 0.1 mL DMSO was added to each well. Absorbance was measured at 570 nm using a Mindray MR-96A microplate reader (Vacutec, Hamburg, Germany), with DMSO as a blank.

2.7 Caspase 3/7 Assay

The Muse™ caspase-3/7 kit was used to quantify the apoptosis and membrane permeability at various stages of apoptosis, using the activity of caspase 3/7 and a dead cell dye. Cells were prepared and treated as described in Section

2.6. After incubating for 48 h, cells were washed with PBS, trypsinized, and 50 µL of assay buffer (1×) was added. The mixture was vortexed, followed by the addition of 5 µL caspase 3/7 reagent. Cells were incubated at 37 °C for 30 min, followed by the addition of 150 µL of caspase 7-AAD working solution. Cells were incubated in the dark at room temperature for 5 min, followed by evaluation of caspase activity using a Muse™ cell analyzer (Luminex, Austin, TX, USA).

2.8 NanoBRET®-TE Intracellular Kinase Assay

The kinase assay was performed according to the manufacturer's protocol. The wild-type and transformed cells were prepared and treated as previously. After 48 h of incubation, the cells were washed with PBS, trypsinized, and the cell density was adjusted to 2×10^5 cells/mL in medium. Approximately 85 µL of cell suspension was dispensed into each well of a white 96-well plate. Thereafter, 5 µL of a complete 20× NanoBRET® tracer reagent (in 100% DMSO) was added. The plate was shaken at 900 rpm for 15 s, followed by incubation at 37 °C for 2 hours. The plates were equilibrated to room temperature for 15 min. The 3× complete substrate and inhibitor solution was prepared by mixing 30 µL of Nano-Glo® substrate, 10 µL of NanoLuc inhibitor, and 4960 µL of assay medium. Approximately 50 µL of this solution was added to each well and incubated at room temperature for 2–3 minutes before analysis. The GloMax® Discover System (Promega Biosystems, Sunnyvale, CA, USA) was used to assess the kinase activity by measuring the donor emission wavelength (450 nm) and the acceptor emission wavelength (610 nm). The kinase activity was calculated as the BRET ratio, which is a unitless value indicating the extent of energy transfer between a donor and acceptor molecule. A high BRET ratio is indicative of a stronger interaction or more efficient substrate phosphorylation, making this ratio a reliable proxy for kinase activity without the need for invasive sampling or endpoint quantification.

2.9 Oxidative Stress Assay

The Muse™ oxidative stress assay was used to quantify reactive oxygen species (ROS) in both wild-type and transformed cells, both before and after treatment. The cells were cultured under the conditions previously described. Once the cells reached the desired confluency, the cells were washed with 100 µL PBS to remove any residual media and non-adherent cells. After washing, the cells were trypsinized with 10–20 µL of trypsin–EDTA and then centrifuged at 300 ×g for 5 min. The pelleted cells were resuspended in 1× assay buffer, with 10 µL of the suspension added to 190 µL of Muse oxidative stress working solution (diluted 1:80 in 1× assay buffer). Cells were vortexed and incubated at 37 °C for 30 minutes before being assessed in a Muse™ cell analyzer (Luminex, Austin, TX, USA) to quantify the ROS (+ or –) cells.

2.10 Multi-Colour DNA Damage Assay

The Muse™ multi-color DNA damage assay assessed the extent of DNA damage resulting from the incorporation of the *LRRK2* G2019S mutation into the genome of the cells, with wild-type cells serving as controls. After 48 h of incubation, the cells were washed in PBS and then trypsinized. Cells were resuspended in 1x assay buffer and centrifuged at 300 ×g for 5 min. The buffer was replaced with 100 µL of fixation buffer, and the sample was incubated at room temperature for 10 minutes and then centrifuged again. The supernatant was removed, and the cells were centrifuged in 100 µL of ice-cold permeabilisation buffer. The cells were then resuspended in 200 µL of assay buffer, and 5 µL of 20× anti-phospho-ATM and 5 µL of 20× anti-phospho-histone were added. Cells were incubated at room temperature in the dark for 30 min, and DNA damage was assessed in a Muse™ cell analyzer (Luminex, Austin, TX, USA).

2.11 Mitopotential Assay

The Muse™ mitopotential kit (Catalog No. MCH100110, Luminex, Austin, TX, USA) assessed mitochondrial stress in transformed and wild-type HEK293 and SH-SY5Y cells. Cells were incubated as previously described, followed by a PBS wash to remove any unwanted debris. Cells were then trypsinized and resuspended in 1× assay buffer to a final cell concentration of 2×10^5 cells/mL. A total of 95 µL of the mitopotential working solution (1:1000 in 1× assay buffer) was added to 100 µL of cell suspension. Cells were vortexed for 3–5 s and incubated at 37 °C for 20 min. Thereafter, 5 µL of the Muse mitopotential 7-AAD reagent was added, the sample was mixed and incubated at room temperature for 5 min, before analysis in the Muse™ cell analyzer (Luminex, Austin, TX, USA).

2.12 Statistical Analysis

All experiments were performed in biological triplicate, unless otherwise stated. Data were analyzed using GraphPad Prism version (ver. 9.0, GraphPad Software Inc., San Diego, CA, USA), and the results are expressed as the mean ± standard deviation (SD). Statistical significance was determined using one-way analysis of variance (ANOVA) followed by Tukey's post hoc test for multiple comparisons. A p-value < 0.05 was considered statistically significant.

3. Results

3.1 Synthesis, Characterization, and siRNA Binding Studies

The confirmation of the synthesis of EGB–PLL–SLNPs and H_2O–PLL–SLNPs, as well as binding studies, was previously described by the authors [22]. The results from UV-vis spectroscopy indicated successful conjugation of PLL to SLNPs (**Supplementary Fig. 1**), with

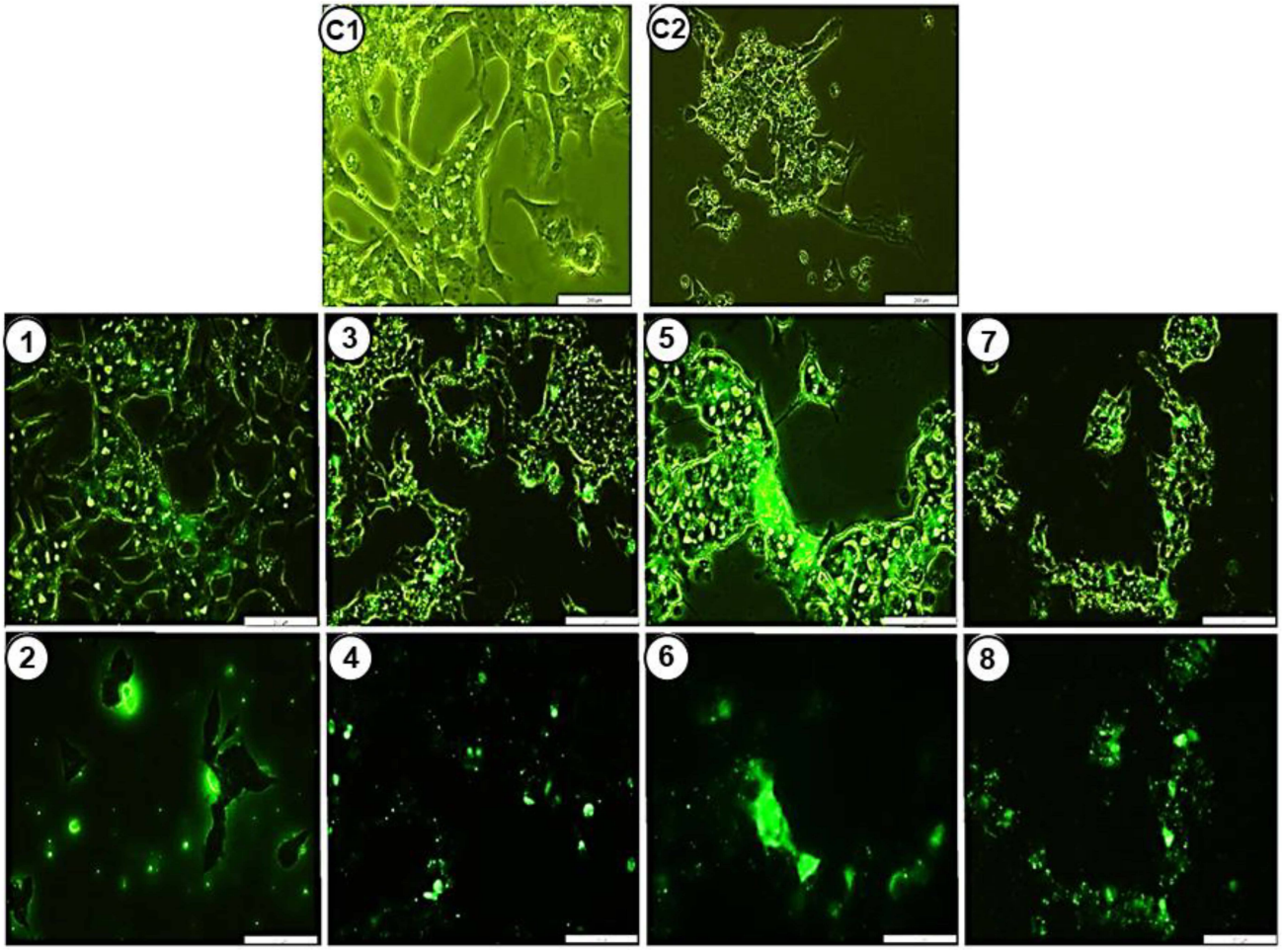

Fig. 1. Fluorescent images of the cellular uptake in SH-SY5Y cells. (C1) Control untreated SH-SY5Y cells. (C2) control Block-IT™ oligo not complexed to the SLNPs. (1–2) oligo:EGB–PLL–SLNPs (1:1 w/w); (3–4) oligo:EGB–PLL–SLNPs (2:1 w/w); (5–6) oligo:H_2O–PLL–SLNPs (1:1 w/w); (7–8) oligo:H_2O–PLL–SLNPs (2:1 w/w). The cells were visualized at 100× magnification. Scale bar = 200 µm. SLNPs, solid lipid nanoparticles; EGB-PLL-SLNPs, Ginkgo biloba leaf extract synthesized poly-L-lysine-solid lipid nanoparticles.

EGB-synthesized SLNPs showing a bathochromic shift, suggesting enhanced interactions compared to the water-based SLNPs. The FTIR analysis confirmed the successful encapsulation of EGB within the SLNPs (**Supplementary Fig. 2**), exhibiting characteristic peaks for O–H and C–H stretching, which corresponded to the incorporation of the aliphatic and phenolic components of EGB. DLS revealed hydrodynamic sizes below 200 nm (**Supplementary Table 1**), suitable for biomedical applications, with the EGB–PLL–SLNPs showing a size of 93.2 nm and a high positive zeta potential (>35 mV), indicating excellent colloidal stability. Transmission electron microscopy (TEM) supported these findings (**Supplementary Fig. 3**), illustrating spherical NPs with no morphological changes upon conjugation with PLL [22]. Overall, the analyses confirmed that the EGB–PLL–SLNPs are stable, well-dispersed, and within the size range for effective cellular uptake.

The intercalation, binding, and protection assays demonstrated the strong ability of the EGB–PLL–SLNPs to bind and protect siRNA effectively (**Supplementary Figs. 4,5,6**). In the intercalation assay, the EGB–PLL–SLNPs achieved 77.78% siRNA compaction, which was slightly better than the H_2O–PLL–SLNPs at 73.60%, indicating efficient quenching of EtBr fluorescence as the NPs bound to the siRNA. The band-shift assay confirmed optimal binding of the EGB–PLL–SLNPs at 0.4:1 (NP:siRNA, w/w) and the H_2O–PLL–SLNPs at a lower ratio of 0.2:1 (w/w). The EGB–PLL–SLNPs also efficiently protected the siRNA from RNase A-mediated degradation compared to the naked siRNA control, which was completely degraded. The integrity and stability of the nanocomplexes were maintained, showing potential for future *in vivo* applications. These findings underscore the efficiency of the EGB–PLL–SLNPs as a siRNA delivery system.

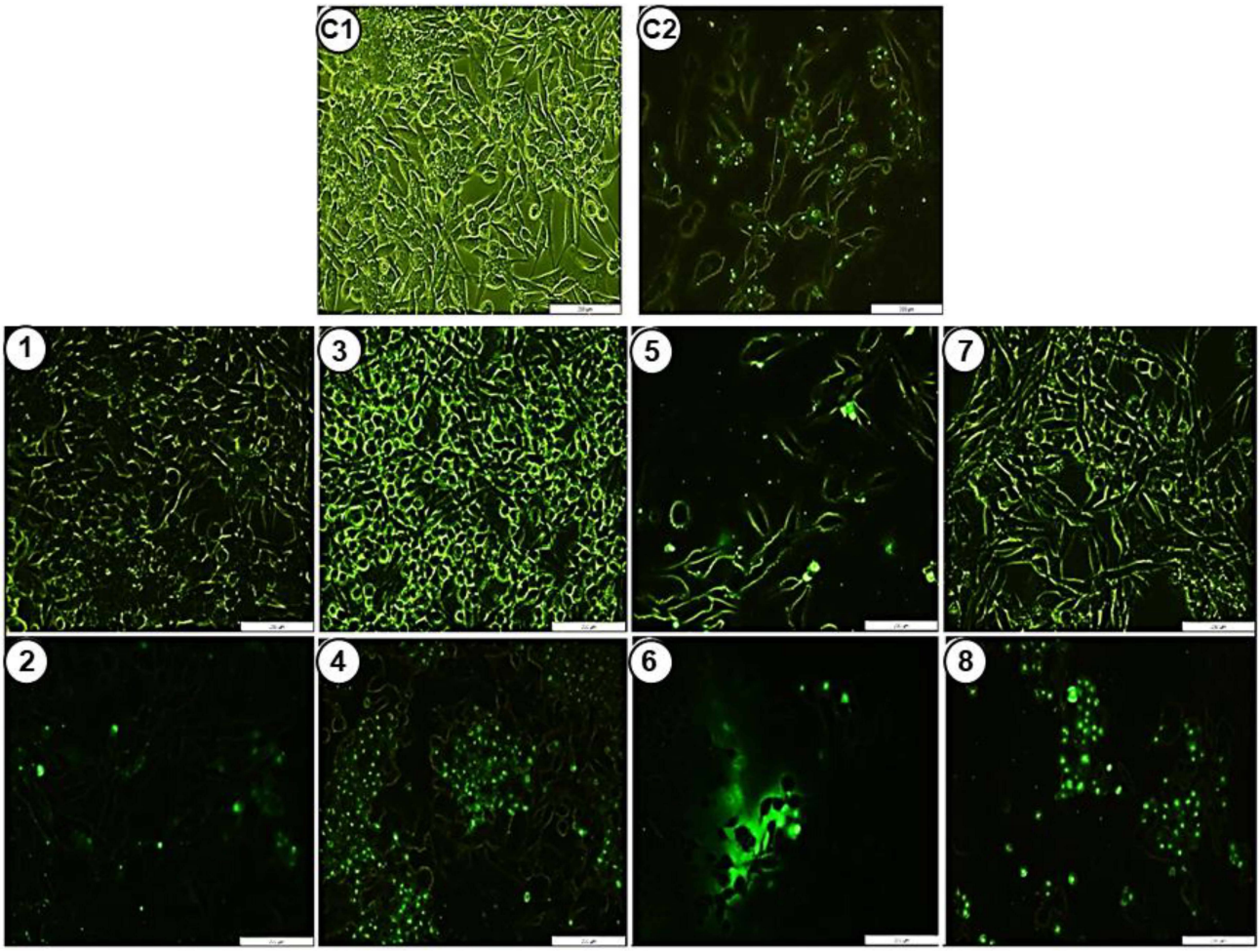

Fig. 2. Fluorescent images of the cellular uptake in HEK293 cells. (C1) Control untreated HEK293. (C2) Control Block-IT™ oligo did not complex to the SLNPs; (1–2) oligo:EGB–PLL–SLNPs (1:1 w/w); (3–4) oligo:EGB–PLL–SLNPs (2:1 w/w); (5–6) oligo:H_2O–PLL–SLNPs (1:1 w/w); (7–8) oligo:H_2O–PLL–SLNPs (2:1 w/w). The cells were visualized at 100× magnification. Scale bar = 200 µm.

3.2 Cellular Uptake: BLOCK-iT™ Fluorescent Oligo Assay

The BLOCK-iT assay was utilized to assess the cellular uptake of the SLNPs in both the transformed SH-SY5Y and HEK293 cells expressing the *LRRK2* G2019S mutation. Fluorescence intensity served as a measure of cellular internalization of the SLNPs (Figs. 1,2). No fluorescence was observed in the transformed SH-SY5Y control cells (Fig. 1 (image C1)). In contrast, the naked BLOCK-iT Oligo produced visible fluorescence with accumulation noted around the perinuclear region, suggesting active endocytic uptake, with a fluorescence intensity of 3290.56 RFU/mg protein (Fig. 3). The EGB–SLNPs (1:2 w/w) displayed increased cellular uptake with a uniform fluorescence within the cytoplasm and accumulation in the perinuclear region (25,247.04 RFU/mg protein) (Fig. 3). Meanwhile, the best uptake for the H_2O–PLL–SLNPs was noted for the 2:1 (w/w) ratio, with fluorescence observed in the cytoplasm (18,579.83 RFU/mg protein). A similar trend was observed in HEK293 cells, as shown in SH-SY5Y cells (Figs. 2,3). Overall, greater cellular uptake was noted at the 2:1 ratio of EGB-PLL-SLNPs (23,879.2 RFU/mg protein), with uniformly distributed SLNPs within the cytoplasm (Fig. 2 (images 3 and 4)). Overall, successful uptake was demonstrated by both SLNPs, with the EGB–PLL–SLNPs demonstrating improved cellular uptake compared to the H_2O–PLL–SLNPs.

3.3 Cytotoxicity

The MTT assay was employed to quantify cell viability. The results indicated that the SLNPs were well tolerated in both SH-SY5Y and HEK293 transformed cells (Fig. 4).

A notable difference in cellular viability was observed between the EGB–PLL–SLNPs and the H_2O–PLL–SLNPs. The EGB–PLL–SLNPs exhibited a cell viability greater than 98% in the SH-SY5Y cells, while the H_2O–PLL-SLNPs showed a viability of 79% (Fig. 4A). Similarly, the EGB–PLL–SLNPs demonstrated a cellular viability of over

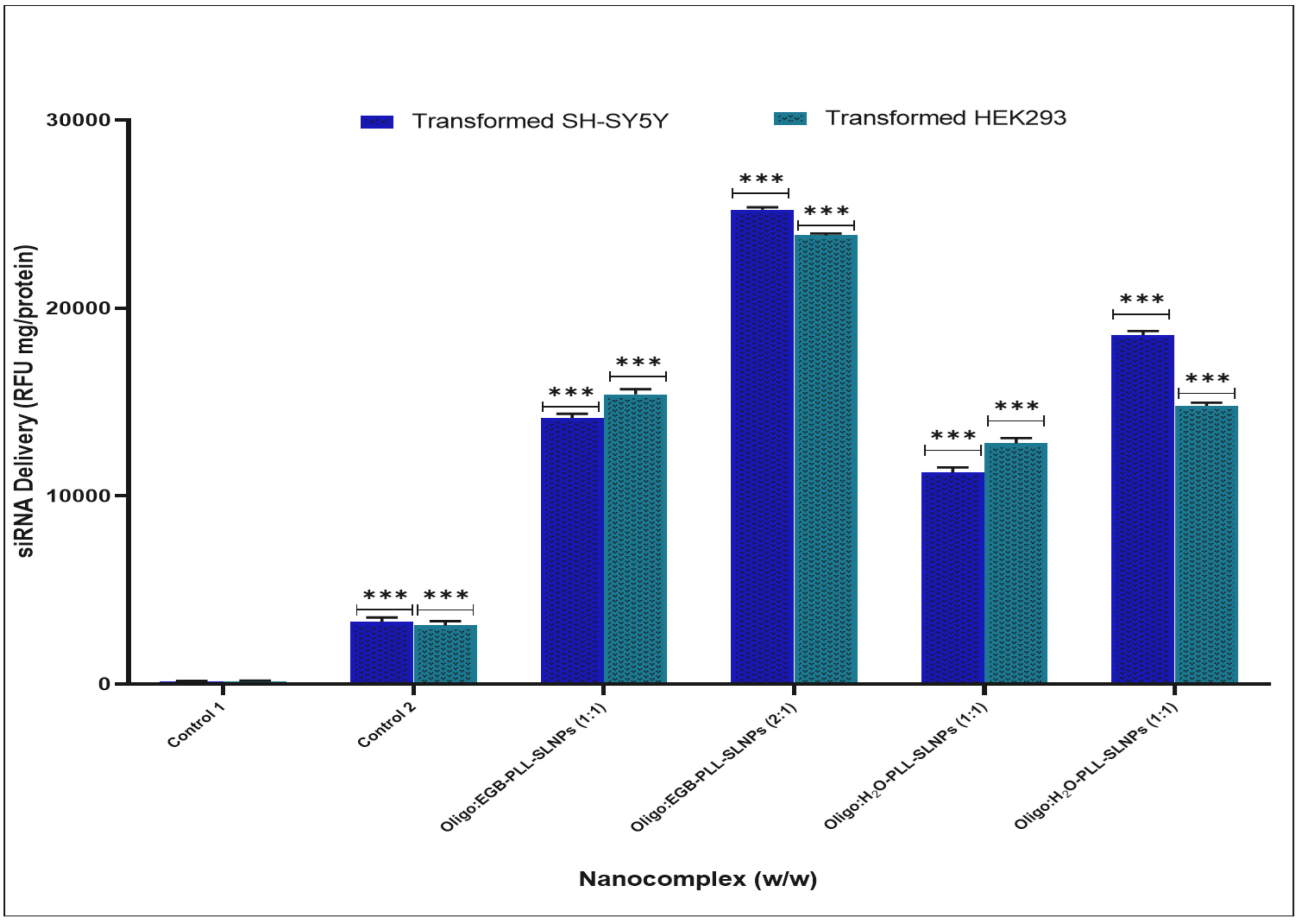

Fig. 3. The relative fluorescence levels for the cellular uptake of the oligo:PLL–SLNPs in the transformed SH-SY5Y and HEK293 cells. Control 1 = cells only; control 2 = Free BLOCK-iT™ Fluorescent Oligo. Data are presented as the mean ± standard deviation (n = 3); *** $p < 0.001$.

92% in the HEK293 cells, compared to 87% for the H_2O–PLL–SLNPs (Fig. 4B). These findings highlight the biocompatibility of EGB–PLL–SLNPs, especially in neuroblastoma cells. Thus, EGB enhances cellular uptake and contributes to increased cell viability.

3.4 Caspase 3/7 Assay

The caspase 3/7 assay data corroborated the MTT assay results. The caspase 3/7 assay quantifies apoptosis using a substrate that, upon cleavage by active caspases 3/7, promotes a fluorescent signal [24]. The cell viability in the transformed SH-SY5Y and HEK293 cells was >87% and 96%, respectively (Table 1 and Fig. 5). In the SH-SY5Y cells (Fig. 5A), the control group (cells only) presented a baseline viability of 95%, with less than 2% of the cells being apoptotic. The RNA control exhibited a decline in viability (87%) and an increase in apoptosis (11%). Treatment with EGB–PLL–SLNPs significantly improved cell viability (98%) and reduced apoptosis (1%). In contrast, treatment with H_2O–PLL–SLNPs showed lower viability (94%) and higher apoptosis (2%).

In HEK293 cells (Fig. 5B), the control cells exhibited high viability, with viability noted in approximately 99% of the cells, while 1% of the cells were apoptotic. However, unlike the SH-SY5Y cells, the RNA control showed improved viability (>99%) with minimal apoptosis. The EGB–PLL–SLNPs resulted in high cell viability (>99%) and low levels of apoptosis. The H_2O–PLL–SLNPS promoted cell viability, which was slightly lower (96%), and increased apoptosis. These findings further confirm the safety and efficiency of EGB–PLL–SLNPs as a therapeutic delivery vehicle.

3.5 Gene Silencing: Kinase Activity Assay

This assay confirmed the potential of the therapeutic siRNA:PLL–SLNPs in targeting and silencing the *LRRK2* G2019S mutation. The *LRRK2* G2019S mutation is widely reported to cause a pathological increase in kinase activity, contributing to the progression of PD [25].

Notably, there was increased baseline kinase activity in the control transformed SH-SY5Y cells compared to the wild-type cells (Fig. 6). Moreover, the kinase activity increased 1.6-fold (from 0.0236 to 0.0378). Treatment

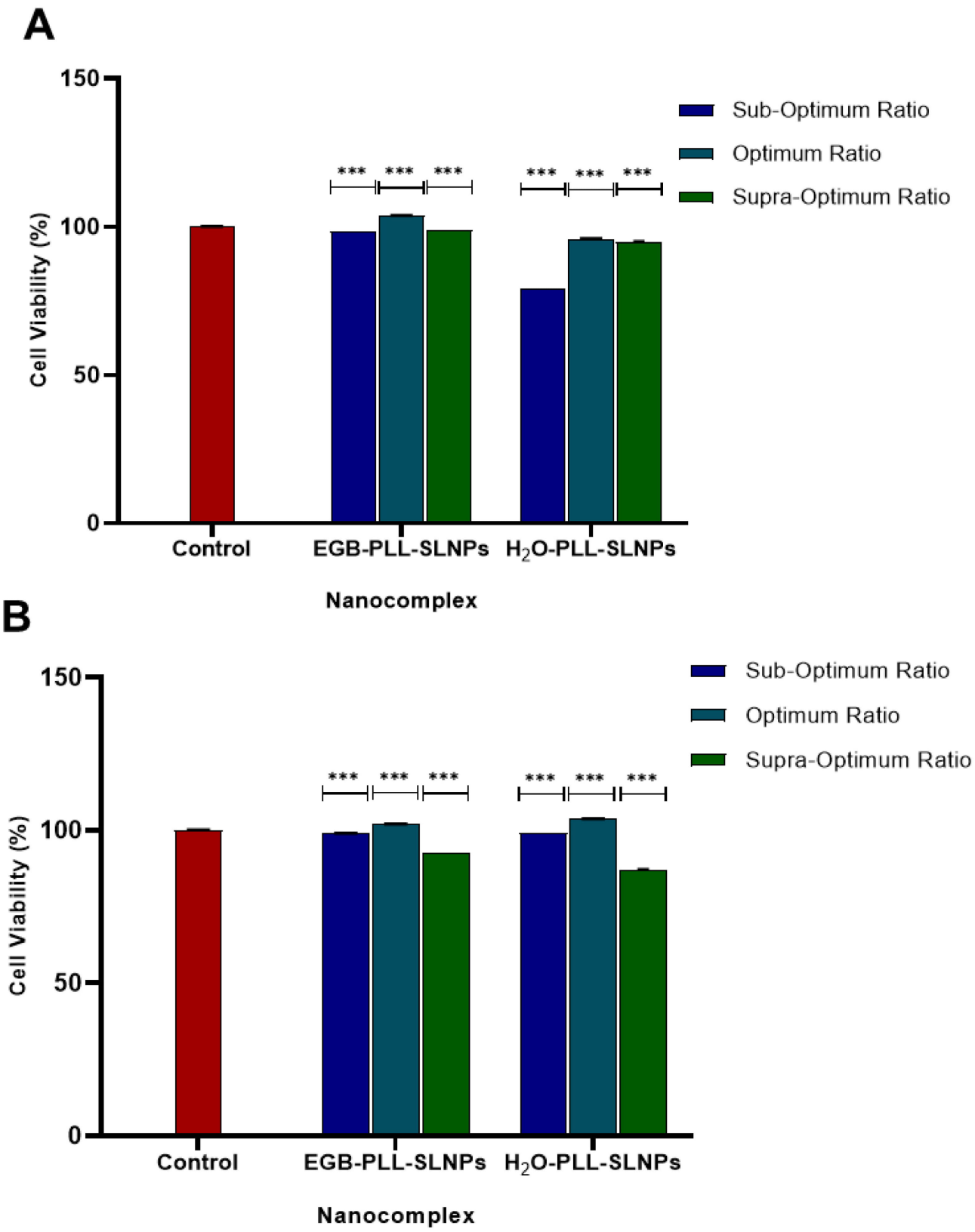

Fig. 4. The MTT cytotoxicity assay in the transformed (A) SH-SY5Y and (B) HEK293 cells. Data are represented as the mean ± standard deviation (n = 3). ***$p < 0.001$ between the corresponding mean of each suboptimum, optimum, and supra-optimum nanocomplexes and the positive control is considered statistically significant (Tukey's multiple comparisons test).

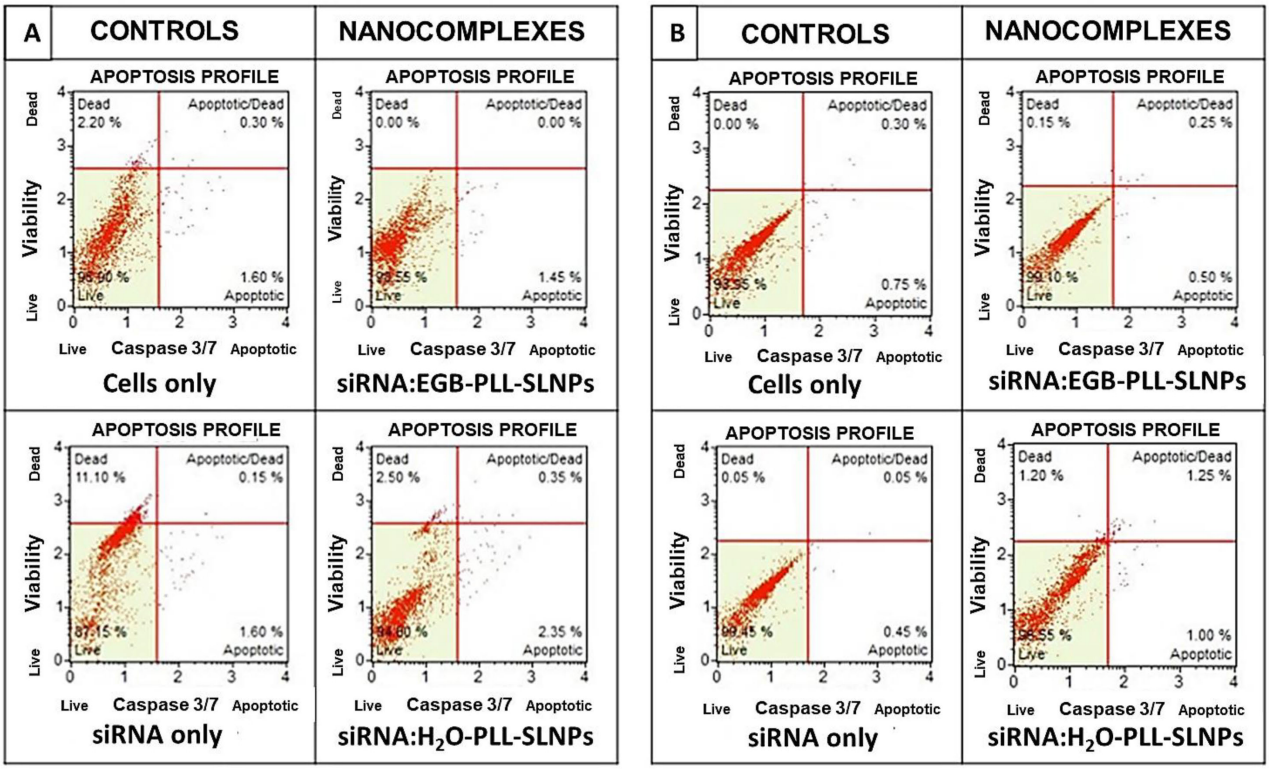

Fig. 5. Caspase 3/7 assay in (A) SH-SY5Y and (B) HEK293 cells. The graph illustrates the apoptotic response of the cells after treatment with siRNA:EGB–PLL–SLNPs and siRNA:H_2O–PLL–SLNPs.

Table 1. Results obtained from the multi-color DNA damage assay with the level of DNA damage in wild-type and transformed SH-SY5Y and HEK293 cells.

Wild type SH-SY5Y cells					
	Negative	p-ATM (single pos.)	Double-strand DNA breaks	p-H2A.X (single pos.)	Total DNA damage
Cells only	71.58%	8.42%	13.68%	6.32%	28.42%
Naked RNA	73.76%	7.80%	12.77%	5.67%	26.24%
siRNA:EGB–PLL–SLNPs	79.55%	6.82%	4.55%	9.09%	20.45%
siRNA:H_2O–PLL–SLNPs	77.36%	9.42%	5.66%	7.55%	22.64%
Transformed SH-SY5Y cells					
	Negative	p-ATM (single pos.)	Double-strand DNA breaks	p-H2A.X (single pos.)	Total DNA damage
Cells only	33.78%	48.65%	16.22%	1.35%	66.22%
Naked RNA	38.15%	51.41%	9.64%	0.80%	61.85%
siRNA:EGB–PLL–SLNPs	66.83%	13.86%	8.91%	10.40%	33.17%
siRNA:H_2O–PLL–SLNPs	55.75%	16.37%	21.24%	6.64%	44.25%
Wild Type HEK293 cells					
	Negative	p-ATM (single pos.)	Double-strand DNA breaks	p-H2A.X (single pos.)	Total DNA damage
Cells only	83.33%	13.89%	2.78%	0.00%	16.67%
Naked RNA	83.52%	13.19%	2.20%	1.10%	16.48%
siRNA:EGB–PLL–SLNPs	88.33%	10.00%	0.00%	1.67%	11.67%
siRNA:H_2O–PLL–SLNPS	84.40%	7.34%	0.92%	7.34%	15.60%
Transformed HEK293 cells					
	Negative	p-ATM (single pos.)	Double-strand DNA breaks	p-H2A.X (single pos.)	Total DNA damage
Cells only	51.74%	1.74%	0.29%	46.22%	48.26%
Naked RNA	60.61%	39.39%	0.00%	0.00%	39.39%
siRNA:EGB–PLL–SLNPs	81.03%	17.24%	1.72%	0.00%	18.97%
siRNA:H_2O–PLL–SLNPS	64.18%	2.64%	0.00%	33.19%	35.82%

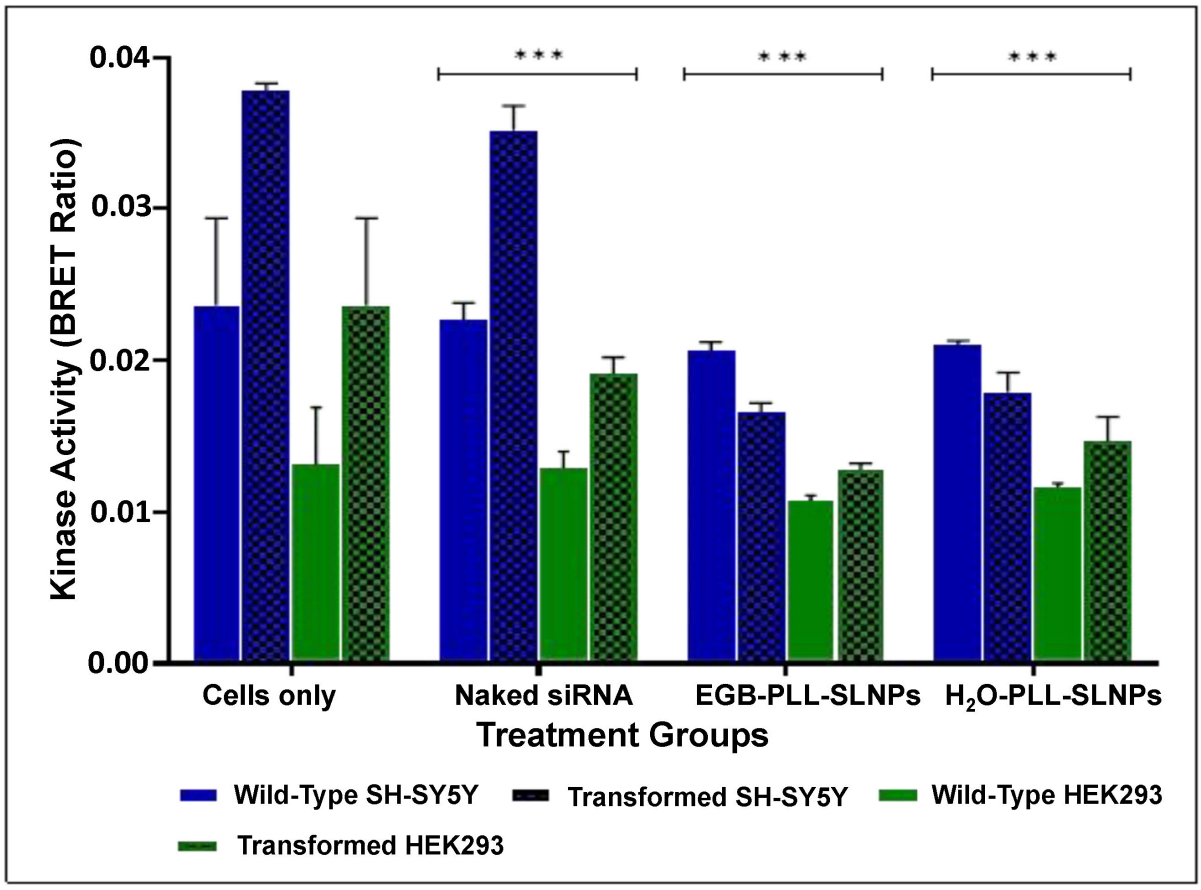

Fig. 6. Impact of therapeutic siRNA-conjugated EGB–PLL–SLNPs and H_2O–PLL–SLNPs on kinase activity in wild-type and *LRRK2* G2019S transformed SH-SY5Y and HEK293 cells. Kinase activity was measured using the intracellular kinase TE assay (Promega), and the results are expressed as BRET ratios. *** $p < 0.001$.

with the naked siRNA did not significantly alter the kinase activity, suggesting that the siRNA may have been degraded within the cells. The EGB–PLL–SLNPs and H_2O–PLL–SLNPs promoted a remarkable 56% and 52% reduction in kinase activity, respectively. A similar increase in kinase activity (1.8-fold change) was observed in the HEK293 cells (Fig. 6). The EGB–PLL–SLNPs and H_2O–PLL–SLNPs caused slightly lower reductions in kinase activity of 45% and 38%, respectively.

The efficiency of the EGB–PLL–SLNPs in reducing kinase activity, again, highlights the potential of these SLNPs as effective therapeutic delivery systems to mitigate the effects of the *LRRK2* G2019S mutation in PD.

3.6 Oxidative Stress

The oxidative stress assay was conducted in the wild-type and transformed SH-SY5Y and HEK293 cells using the Muse oxidative stress kit (Fig. 7). A baseline of 14% ROS (+) cells was observed in the SH-SY5Y wild-type cells, with a significant decrease following the administration of the nanocomplexes. The EGB–PLL–SLNPs produced the greatest decline in ROS (+) cells to around 6% (Fig. 7A). The transformed SH-SY5Y cells showed an increase of 14% in ROS (+) control cells. Treatment with the EGB-based nanocomplexes produced a slight improvement, with a 14% reduction in oxidative stress compared to the H_2O-based counterparts (17%). The normalization studies showed that the EGB-based nanocomplexes could reduce oxidative stress to baseline levels after 48 h (Fig. 7B).

A similar trend was observed in the HEK293 cells (Fig. 8). The control cells demonstrated a less pronounced increase in ROS (+) cells from the wild-type to transformed cells. Although this increase was lower, it was sufficient to validate successful transfection. Likewise, the EGB-based nanocomplexes produced a slightly improved effect, with a 0.5% reduction in oxidative stress compared to their H_2O-based counterparts (3%). These results demonstrate the ability of the nanocomplex to effectively target and silence the *LRRK2* G2019S mutation, with the EGB providing enhanced antioxidant activity. Normalization indicated a significant reduction in oxidative stress levels compared to the baseline recorded for the wild-type.

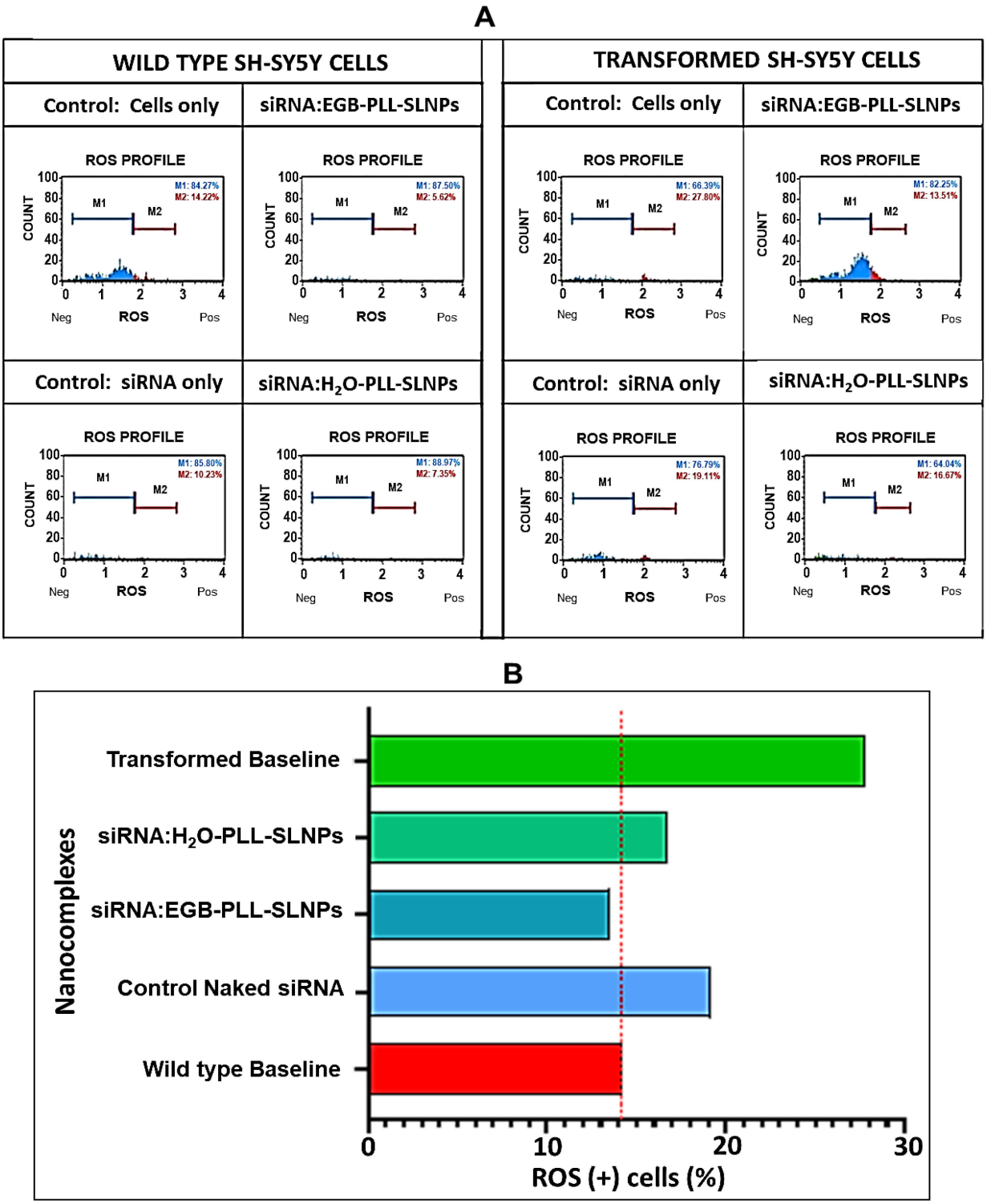

Fig. 7. Oxidative stress analysis of therapeutic nanocomplexes on wild-type and transformed SH-SY5Y cells. (A) Flow cytometry profiles. (B) The normalization studies compared the ROS (+) cells between the transformed SH-SY5Y cells post-treatment and the baseline of the wild-type control.

3.7 DNA Damage Assay

The DNA damage assay was conducted on wild-type and transformed SH-SY5Y and HEK293 cells. The results are presented in Table 1, Fig. 9, and **Supplementary Fig. 7**. The DNA damage assay results were visualized using flow cytometric dot plots, which show total H2AX expression on the Y-axis and phosphorylated H2AX (p-H2AX) on the X-axis. Cells located in the upper right quadrant (double-

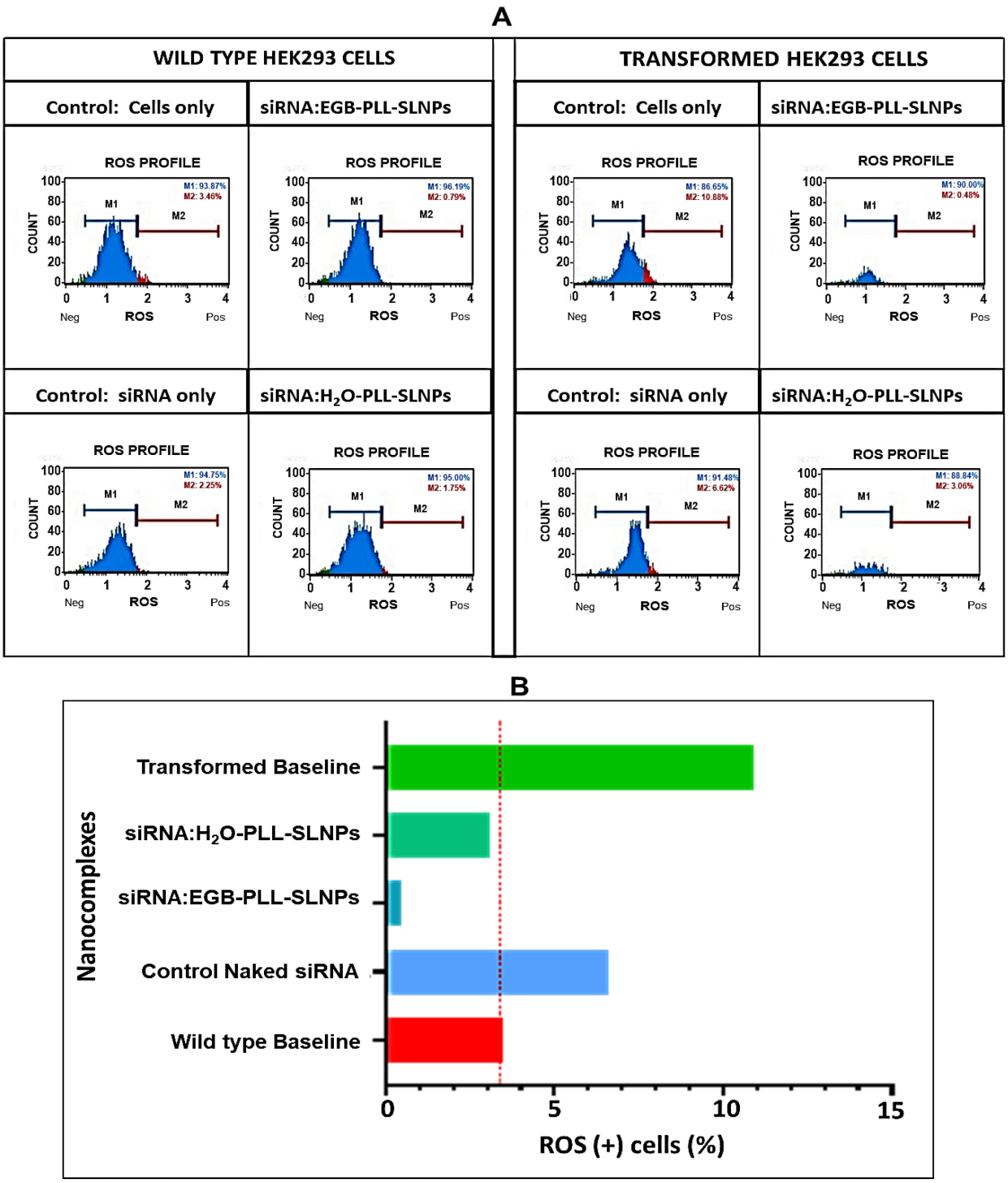

Fig. 8. Oxidative stress analysis of therapeutic nanocomplexes on wild-type and transformed HEK293 cells. (A) Flow cytometry profiles. (B) The normalization studies compare the ROS (+) cells between the transformed HEK293 cells post-treatment and the baseline of the wild-type control.

positive for total and p-H2AX) represent the positive DNA damage population. The distribution of cells across these quadrants provides insights into genotoxic stress and the activation of the repair pathway.

A baseline DNA damage level of 28% was observed in the wild-type SH-SY5Y control cells, indicating significant DNA damage before transformation with the *LRRK2* G2019S plasmid. Naked siRNA treatment did not promote significant DNA damage (26%). In comparison, the EGB-conjugated nanocomplexes showed lower DNA damage than the H_2O-based nanocomplexes.

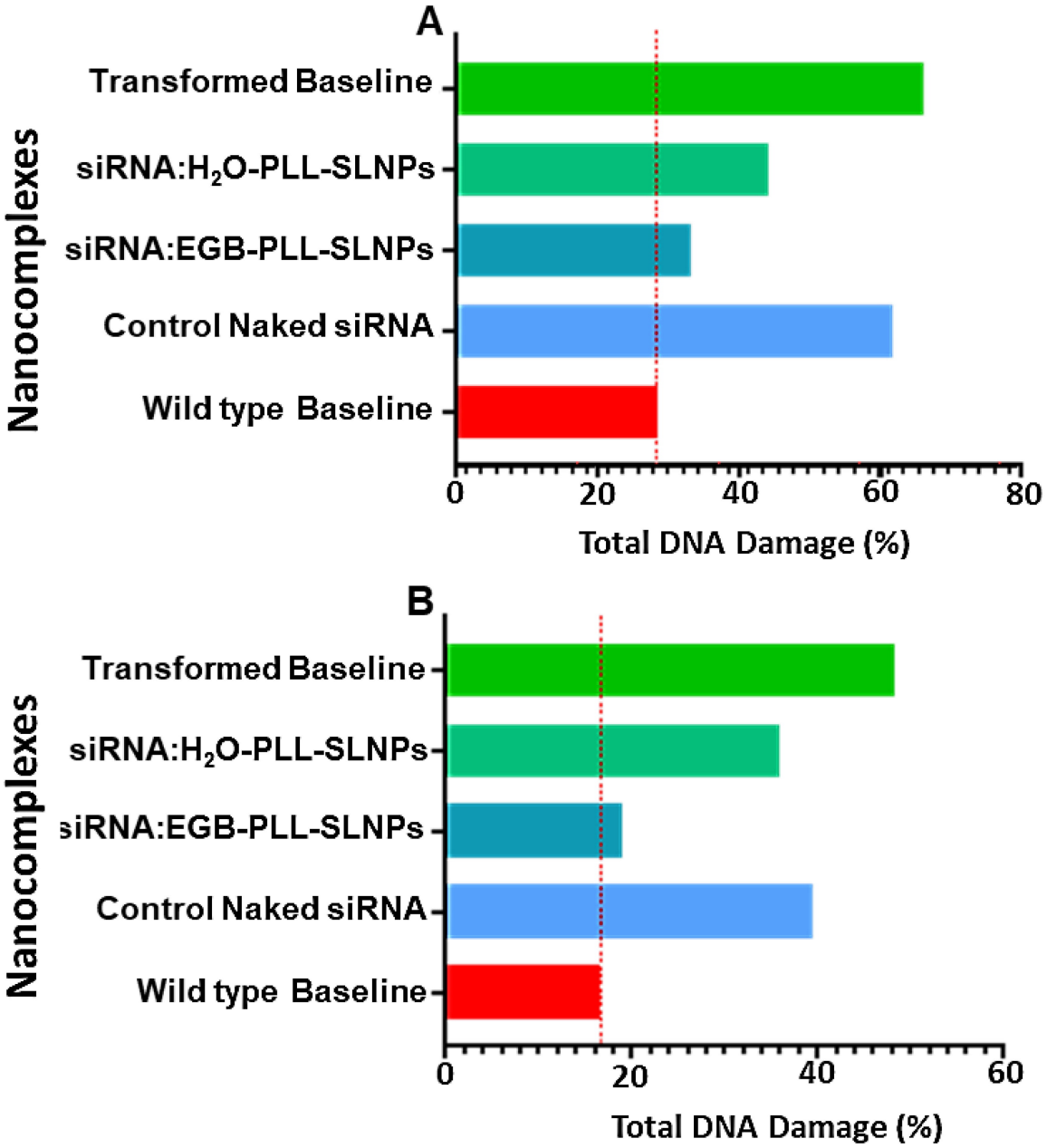

Fig. 9. Graphical representation of DNA damage studies. Normalization studies of the comparison for the total percentage of cells with DNA damage (%) (A) between the transformed SH-SY5Y cells post-treatment and the wild-type control baseline, as well as (B) the transformed HEK293 cells post-treatment and the wild-type control baseline.

A similar trend was noted in the transformed SH-SY5Y cells, with the baseline control presenting increased DNA damage at 48.65%, highlighting the detrimental effect of the transformation on the neuroblastoma cells. Treatment with naked siRNA increased DNA damage to 61%, while the EGB-conjugated nanocomplexes reduced DNA damage to 33%, compared to 44% for the H_2O-nanocomplexes. Importantly, a 10% increase in p-H2A.X levels was observed in cells treated with the EGB-conjugated nanocomplex, providing insight into the ability of this complex to activate DNA repair mechanisms.

In the wild-type HEK293 cells, the initial DNA damage was 17%, with no change in p-H2A.X levels, indicating that no repair mechanisms were activated before treatment. A reduction in DNA damage was observed for the naked siRNA treatment. The EGB-conjugated nanocomplexes produced a greater reduction than the H_2O-nanocomplexes. Meanwhile, the baseline DNA damage increased to 48% in the transformed HEK293 cells, confirming successful transfection. Naked siRNA and H_2O-nanocomplexes showed similar DNA damage levels, while the EGB-conjugated nanocomplexes produced a more sig-

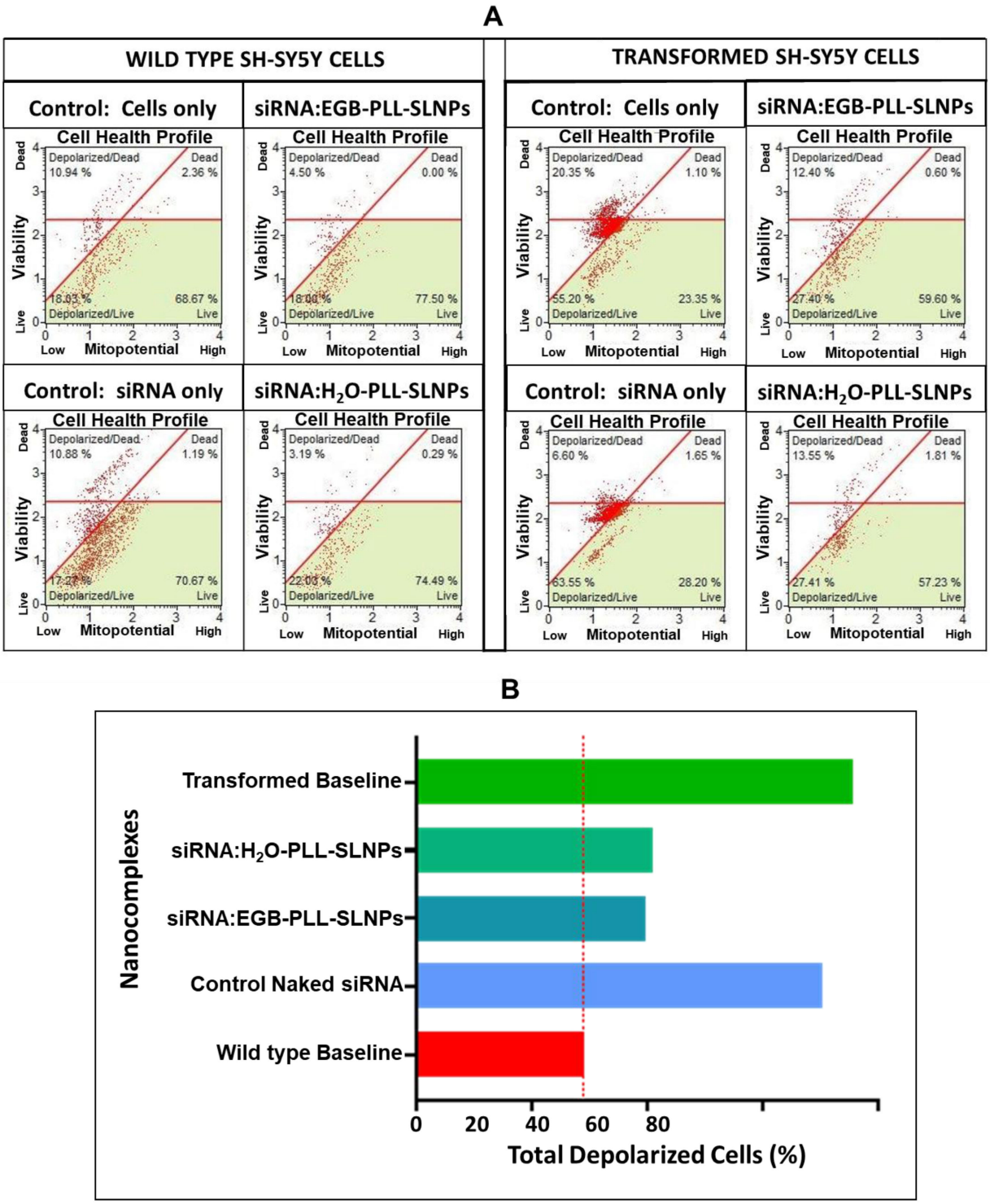

Fig. 10. The mitopotential analysis in wild-type and transformed SH-SY5Y cells. (A) The flow cytometry profiles analysis of the various therapeutic groups. (B) The normalization studies present a comparison of the total depolarized cells (%) between the transformed SH-SY5Y cells post-treatment and the wild-type control baseline.

nificant reduction to 19%. Protein normalization studies in both cells showed slight variations in the reductions.

3.8 Mitopotential Assay

The *LRRK2* G2019S mutation is known to induce mitochondrial stress, leading to significant cellular damage. The mitopotential assay was utilized to assess mitochon-

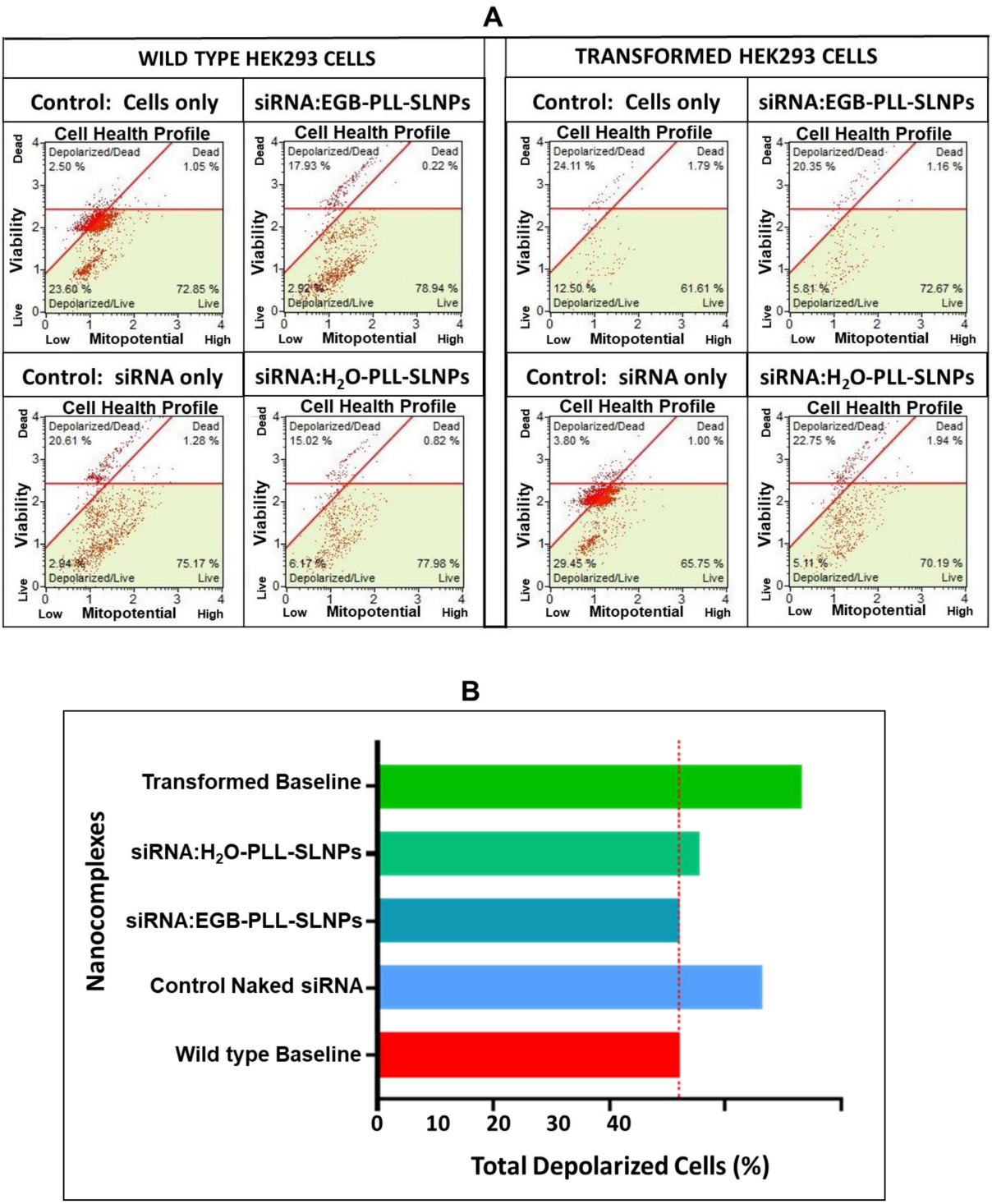

Fig. 11. The mitopotential analysis in wild-type and transformed HEK293 cells. (A) The flow cytometry profiles analysis of the various therapeutic groups. (B) Normalization studies of a comparison of the total depolarized cells (%) between the transformed HEK293 cells post-treatment and the wild-type control baseline.

drial health and stress in both transformed and wild-type cells.

In the SH-SY5Y cell line (Fig. 10), a total of 69% live cells were found in the control group (wild-type cells only), with a total depolarization cell count of 29%, serving as a baseline for comparing therapeutic outcomes. Treatment with naked siRNA did not produce a significant improvement.

Treatment with the nanocomplexes reduced mitochondrial damage, with no major differences in therapeutic efficacy observed among the different nanocomplexes. The transformed SH-SY5Y cells exhibited a significant increase in mitochondrial dysregulation, with 76% of cells being depolarized. The naked siRNA group showed a 5% decline in depolarized cells. Both treatment groups were effective in decreasing the level of damage to around 40%. These results were above the wild-type control baseline, indicating good mitochondrial recovery.

The DNA damage presented in the HEK293 cells (Fig. 11) was similar to that in the SH-SY5Y cells. However, a lower initial depolarization was noted in transformed HEK293 cells compared to SH-SY5Y cells. The increase in depolarization to 37% validated the successful siRNA transfection. The naked siRNA did not significantly affect the cell health, with the nanocomplexes producing similar results. These results were observed to be less than 2% above the wild-type baseline, indicating a nearly normalized mitopotential following treatment.

4. Discussion

The successful synthesis and characterization of the SLNPs were fully described previously by the authors [22]. All SLNPs were of favorable size (<150 nm) and stability (zeta potentials >35 mV) for cellular studies. These results, together with successful siRNA binding and protection studies, confirmed the potential of these SLNPs as suitable vehicles for gene delivery [22]. The EGB–PLL–SLNPs showed a greater ability to facilitate cellular uptake compared to their H_2O-based counterparts. The increased uptake at a ratio of 1:2 (w/w) underscored the dose-dependent nature of the internalization of the SLNPs in both neuroblastoma and embryonic kidney cells. For the biosynthesized SLNPs, this can be attributed to the bioactive components of EGB, such as flavonoids and terpenoids, which possess the ability to integrate into lipid bilayers, increasing the fluidity and permeability of the membrane and enhancing cellular uptake [26]. Endocytosis could also have been stimulated by the ginkgolides in the EGB, leading to increased internalization of the SLNPs [27]. Moreover, compounds such as quercetin and kaempferol can interact with cell surface receptors, facilitating uptake through receptor-mediated endocytosis and thereby achieving a more targeted and efficient uptake, while reducing off-target effects [28]. However, while the presence of bioactive flavonoids and terpenoids, such as EGB, is well established in the literature, this study did not employ high-performance liquid chromatography (HPLC) to quantify their individual concentrations. The primary aim of adding the EGB was to leverage its green-synthesis capabilities as a reducing and stabilizing agent during SLNP formation. The functional outcomes were presented as comparative observations, with the results obtained between the biologically synthesized (EGB–PLL–SLNPs) and non-biologically synthesized (H_2O–PLL–SLNPs) nanocomplexes, rather than assessing the dose-dependent pharmacology of the EGB compounds.

Furthermore, the stability and protective efficiency of the nanoparticles were evaluated under both storage and physiologically relevant conditions. Band-shift assays were conducted after one year of SLNP storage, demonstrating unchanged binding ratios with the siRNA, indicating the long-term preservation of the integrity of the nanoformulations. Additionally, a nuclease protection assay was conducted, under physiologically relevant conditions, on the SLNPs after one year of storage. The obtained results confirmed that SLNPs effectively protected the siRNA against enzymatic degradation, underscoring the suitability of SLNPs for delivery and clinical translation *in vivo*.

The comparison between cellular uptake in wild-type and transformed cells revealed interesting insights. The transformed cells exhibited greater SLNP uptake compared to the wild-type. This can be attributed to alterations in cellular pathways and increased metabolic activity associated with the *LRRK2* G2019S mutation, particularly the increase in kinase activity that enhances endocytosis and intracellular trafficking [29,30]. This is due to the increased formation and trafficking of extracellular vesicles (EVs), including exosomes. These small membrane-bound vesicles play a crucial role in intracellular communication and transport of molecular cargo. Moreover, the *LRRK2* G2019S mutation promotes the upregulation of genes, such as RAB27B, which are involved in the biogenesis and secretion of EVs [31,32]. Small multivesicular bodies (MVBs) are also formed, which increase the docking sites for the NPs, and enhance cellular uptake [33,34]. This drives the energy-intensive processes of vesicle trafficking, formation, and fusion with target membranes, facilitating internalization and distribution of the SLNPs.

The intracellular delivery of BLOCK-iT fluorescent oligos in this study confirmed that the SLNPs not only entered the cells but also localized within the cytoplasm and perinuclear region, as visualized through fluorescence microscopy. The uniform cytoplasmic distribution of fluorescence strongly suggests successful endosomal escape, which is a critical step for RNAi activity. The combined results obtained from the MTT and caspase 3/7 assays provide a comprehensive overview of the cytotoxicity and apoptotic profiles of the SLNPs, which will affect their therapeutic potential. The SLNPs performed best under optimal binding conditions, highlighting the need to inhibit cytotoxicity at higher concentrations [2]. The EGB–PLL–SLNPs exhibited higher cell viability and lower apoptotic indices *in vitro*, compared to the H_2O–PLL–SLNPs, which showed an increase in the apoptotic index. This highlights the anti-apoptotic properties of the bioactive compounds in EGB, especially the terpenoids such as ginkgolides, which inhibit the release of cytochrome c from the mitochondria, thereby preventing the activation of key apoptosis execu-

tioners, including caspase-3 and 7 [35]. EGB also downregulates the expression of pro-apoptotic proteins, including Bax, and upregulates the expression of anti-apoptotic proteins, such as Bcl-2. Shifting the balance between anti- and pro-apoptotic proteins enhances cell survival and reduces apoptosis [36]. The activation of nuclear factor-kappa B (NF-κB), a transcription factor that promotes the expression of pro-apoptotic and pro-inflammatory genes, is inhibited by EGB, reducing inflammation-induced apoptosis. This is beneficial in neurodegenerative diseases such as PD. The SLNPs, lacking the anti-inflammatory properties exhibited by the EGB, could induce an inflammatory response upon successful uptake and internalization, thereby inducing apoptosis [37].

While the siRNA used in this study was commercially sourced and pre-validated for allele-specific targeting of *LRRK2* G2019S, the proprietary nature of the sequence precluded in-house validation of design features such as off-target profiling or chemical modifications. Instead, therapeutic efficacy and specificity were assessed through downstream functional assays, including kinase activity, mitochondrial integrity, oxidative stress, apoptosis, and DNA damage, all of which were significantly improved following siRNA treatment. Future studies may expand on this by incorporating transcript (reverse transcription quantitative polymerase chain reaction, RT-qPCR) and protein-level (Western blot) validation, and evaluating phospho-Rab10 as a surrogate marker of LRRK2 kinase inhibition.

The *LRRK2* G2019S mutation is reported to increase kinase activity, contributing to the progression of PD [25]. The mutative substitution of glycine with serine at position 2019 enhances the intrinsic catalytic activity of the kinase through structural alterations, conformational changes, and increased autophosphorylation at several residues [29,30]. Consequently, the increase in kinase activity promotes neuroinflammation, synaptic defects, and mitochondrial dysfunction, leading to the loss of mDAs, which is characteristic of PD [25,29]. The kinase activity results provided compelling evidence of the therapeutic potential of the siRNA-bound PLL–SLNPs. A significant reduction in kinase activity was noted in the transformed cells, indicating that the siRNA effectively limited the genetic aberrations caused by the mutation, with the EGB acting synergistically due to the presence of quercetin, kaempferol, and isorhamnetin. These compounds bind to the active sites of kinases, minimizing their ability to phosphorylate substrates, resulting in a significant reduction in kinase activity [38]. The extract can modulate signaling pathways, such as the PI3K/Akt pathway, which intersects with kinase activity, and is involved in cell survival and proliferation. Thus, the inhibition of the PI3K/Akt pathway reduces the activation of downstream kinases [39]. As previously evidenced, EGB can infiltrate the cellular membrane for efficient internalization. Overall, the siRNA:EGB–PLL–SLNPs were effective in silencing the *LRRK2* G2019S mutation by reducing kinase activity close to the wild-type baseline. A study by Nichols *et al.* (2009) [40] reported a 30% reduction in kinase activity using traditional kinase inhibitors [29]. This was corroborated by a study using a nano-delivery system, which achieved a 35% reduction in kinase activity [41]. Furthermore, studies using siRNA to target *LRRK2* have noted a 40–50% decline in kinase activity upon treatment [42,43]. These results align with our findings, highlighting a slightly higher reduction in kinase activity.

While several small-molecule LRRK2 inhibitors have shown efficacy in reducing kinase activity, these inhibitors have also been associated with off-target effects and toxicity. Preclinical and clinical studies have reported adverse events including pulmonary alterations (e.g., type II pneumocyte hypertrophy), renal vacuolation, and immune-related disturbances due to systemic exposure [14,44]. These safety concerns have limited the clinical translation of LRRK2 inhibitors, especially in chronic dosing scenarios. In contrast, our siRNA-loaded SLNP system offers a targeted approach with the potential for reduced systemic toxicity. By delivering gene-silencing cargo directly into affected cells and enabling intracellular release, this platform minimizes off-target organ exposure and immunogenic activation—thus offering a potentially safer and more localized alternative to systemic kinase inhibitors.

The enhanced kinase activity resulting from the *LRRK2* G2019S mutation increases oxidative stress by increasing ROS production, thereby contributing to neuronal damage in PD [45,46]. A notable reduction in ROS levels was observed for both cells, demonstrating the efficacy of these nanocomplexes in reducing oxidative stress. Notably, the elevated ROS levels in the wild-type cells are due to the cancer state of the neuroblastoma cells, which inherently exhibit increased oxidative stress due to heightened metabolic activity [47]. This serves as a baseline for comparative purposes. The ROS (+) levels were reduced to near-normal levels compared to the wild-type baseline, highlighting the potent therapeutic effect of the siRNA in silencing the gene of interest and normalizing elevated pathogenic levels. Similarly, the synergistic activity of the EGB with the siRNA enabled the effective scavenging of free radicals. The antioxidants (terpenoids and flavonoids) in the extract neutralize ROS through electron donation, thereby mitigating oxidative stress within cells [45,46]. These compounds enhance cellular antioxidant defense mechanisms through the upregulation of enzymes, such as superoxide dismutase (SOD) and glutathione peroxidase (GPx), further detoxifying ROS [47].

Studies on varied treatments for PD, with regard to decreasing oxidative stress, have shown varying degrees of effectiveness. Traditional antioxidant therapies, such as coenzyme Q10, have shown a 10% reduction in ROS in clinical trials, which was not substantial enough to yield clinical benefits [48]. Vitamin E supplementation reduced ROS production in an *in vitro* PD study [49], while an

increase in efficacy was noted in a separate study using NP-encapsulated antioxidants [27]. This study observed a significant reduction (>50%) after administering the siRNA:EGB–PLL–SLNPs.

The multi-color DNA damage assay highlighted the differences associated with the mutational event. The elevated levels of p-ATM, double-stranded DNA breaks (DSBs), and p-H2A.X in the transformed cells suggested heightened genomic instability. The *LRRK2* G2019S mutation is known for impairing DNA repair pathways, increasing susceptibility to DNA damage, and permitting the onset of PD through neuronal loss [50]. This leads to the persistent activation of DNA damage checkpoints and neuronal apoptosis, resulting in genomic instability related to PD [51]. The transformed SH-SY5Y cells had higher levels of p-ATM, DSBs, and p-H2A.X, indicating persistent activation of DNA damage responses, genomic instability, and ongoing DNA damage and repair. A significant elevation in damage was noted in the transformed HEK293 cells, particularly in p-H2A.X levels, accompanied by a reduction in p-ATM and DSBs. The siRNA:EGB–PLL–SLNPs were more efficient in reducing DNA damage than the siRNA:H_2O–PLL–SLNPs, providing further evidence of the gene silencing effects through the synergism of EGB and siRNA. A reduction in p-ATM and DSBs indicated a reduced activation of DNA damage response levels due to the significant DNA repair mechanisms. In contrast, increased p-H2A.X levels indicated greater activation of DNA repair mechanisms in response to DNA damage [52]. The p-H2A.X levels were abolished by the siRNA:H_2O–PLL–SLNPs, suggesting an effective repair mechanism. Apart from the aforementioned benefits of EGB, this extract has been shown to modulate chromatin remodeling and facilitate access of repair enzymes to damaged DNA sites [47]. Theoretically, EGB enhances ATP-dependent chromatin remodeling complexes such as the SWI/SNF complex. These complexes alter chromatin structure by displacing nucleosomes and recruiting DNA repair proteins to the damage sites [51,53].

The mitochondrial membrane potential is an indicator of mitochondrial function, reflecting the maintenance of an electrochemical gradient [54]. Due to the increased kinase activity resulting from the mutation, normal mitochondrial function becomes impaired due to fragmentation and an increase in ROS production [44,55]. Mitochondrial trafficking and biogenesis are affected, disrupting the mitochondria along the neuronal axons and resulting in energy deficits at synaptic terminals as well as impaired neuronal function. This increases the vulnerability of the mDAs to degeneration, resulting in PD [56]. Interestingly, increased depolarization was noted in the transformed cells. The nanocomplexes were successful in reducing this damage, but to a lesser extent in the HEK293 cells.

These results further highlight the efficacy of the siRNA in gene silencing and the favorable effects of the EGB–PLL–SLNPs in maintaining mitochondrial integrity. Quercetin and kaempferol from EGB enhance mitochondrial function by stabilizing the mitochondrial membrane and promoting ATP production [57]. Quercetin can improve the activity of complexes I and III in the electron transport chain, simultaneously maintaining the mitochondrial membrane and reducing its dysfunction [58]. Kaempferol protects the mitochondria by promoting the activity of antioxidant enzymes [59]. The compounds in EGB can activate the PGC-1α signaling pathway, leading to an increased expression of nuclear and mitochondrial genes essential for replication, growth, and mitochondrial function [52]. The production of new mitochondria and improvements in overall cellular functionality and energy production are enhanced [60].

Although this study did not directly quantify post-treatment *LRRK2* gene expression levels using qPCR or RNA-sequencing, the specificity and efficacy of the siRNA-mediated knockdown were functionally validated through a comprehensive panel of downstream assays. The *LRRK2* G2019S mutation is known to drive specific pathological phenotypes, including elevated kinase activity, mitochondrial depolarization, oxidative stress, apoptosis, and impaired DNA repair mechanisms, all of which were measured and found to be significantly improved following treatment with siRNA-loaded SLNPs. These phenotypic corrections provide strong support for the specificity of gene silencing. While transcript-level validation remains a valuable future direction, the multi-assay approach performed here provides robust evidence for the mutation-targeted therapeutic effect of the delivery system.

Overall, the siRNA-mediated silencing of the *LRRK2* G2019S mutation decreases kinase activity, creating a cascade effect on other factors influenced by its mutation. This silencing effect complements the antioxidant activity of EGB, providing a dual therapeutic approach for protecting the mitochondria and preventing neuronal loss.

5. Conclusions

This study demonstrated that the siRNA delivery system, utilizing EGB–PLL–SLNPs, effectively silenced the *LRRK2* G2019S mutation and mitigated its adverse effects. The *LRRK2* G2019S mutation leads to increased kinase activity, mitochondrial dysfunction, elevated ROS production, impaired DNA repair mechanisms, and ultimately promotes neuronal loss in PD. Although endosomal markers or trafficking inhibitors were not employed, the significant downstream silencing effects observed support effective cytoplasmic delivery and RNA-induced gene silencing. The EGB–PLL–SLNPs delivery system exhibited remarkable efficacy in targeting and silencing the *LRRK2* G2019S gene, as evidenced by substantial improvements in mitochondrial health and a marked increase in cell viability. Moreover, the system achieved a favorable reduction in ROS levels, DNA damage, and kinase activity. The supe-

rior performance of the EGB–PLL–SLNPs can be attributed to the synergistic effects of the bioactive compounds of EGB, namely, quercetin and kaempferol, which stabilize mitochondrial membrane potential, enhance ATP production, and upregulate genes involved in mitochondrial biogenesis. This dual therapeutic effect, achieved by combining the protective and antioxidant properties of EGB with the gene-silencing capabilities of siRNA, offers a robust and promising approach for managing the pathogenic effects of the *LRRK2* G2019S mutation in PD. This study provides compelling evidence supporting the use of EGB–PLL–SLNPs as a potent and innovative nanosystem, with significant therapeutic outcomes compared to traditional delivery systems, and creates an avenue for advancement in the treatment of PD.

Future research should focus on optimizing the formulation and delivery of EGB–PLL–SLNPs to further enhance their therapeutic efficacy and specificity in targeting the *LRRK2* G2019S mutation. Investigating the long-term effects and stability of these SLNPS *in vivo* will provide valuable insights into their potential clinical applications. Additionally, exploring the combination of EGB–PLL–SLNPs with other therapeutic agents or treatment modalities could produce a novel treatment strategy for PD. The precise mechanisms through which the bioactive compounds in EGB contribute to the observed therapeutic benefits should be investigated. It would be beneficial to expand this research to include other neurodegenerative diseases with similar pathological mechanisms, thereby assessing the broader applicability of this approach. Ultimately, *in vivo* studies in animal models are crucial for validating the safety and efficacy of EGB–PLL–SLNPs, paving the way for their eventual adoption in clinical settings.

Availability of Data and Materials

All data are reported in this paper will also be shared by the lead contact upon request.

Author Contributions

KJ and MS conceptualised and designed the research study. KJ performed the research. MS supervised the study, providing funding, resources and help and advice on experimentation. KJ analyzed the data. KJ wrote the original draft of the manuscript. MS was involved in the review and final editing of the manuscript. Both authors read and approved the final manuscript. Both authors have participated sufficiently in the work and agreed to be accountable for all aspects of the work.

Ethics Approval and Consent to Participate

Not applicable.

Acknowledgment

We acknowledge the advice and technical support from the members of the Nano-Gene and Drug Delivery group.

Funding

Funding was provided by the National Research Foundation, South Africa (grant numbers 129263 and 120455).

Conflict of Interest

The authors declare no conflict of interest.

Supplementary Material

Supplementary material associated with this article can be found, in the online version, at https://doi.org/10.31083/FBE44344.

References

[1] Virreira Winter S, Karayel O, Strauss MT, Padmanabhan S, Surface M, Merchant K, *et al*. Urinary proteome profiling for stratifying patients with familial Parkinson's disease. EMBO Molecular Medicine. 2021; 13: e13257. https://doi.org/10.15252/emmm.202013257.

[2] Przedborski S. The two-century journey of Parkinson disease research. Nature Reviews. Neuroscience. 2017; 18: 251–259. https://doi.org/10.1038/nrn.2017.25.

[3] Schapira AHV, Chaudhuri KR, Jenner P. Non-motor features of Parkinson disease. Nature Reviews. Neuroscience. 2017; 18: 435–450. https://doi.org/10.1038/nrn.2017.62.

[4] Deng H, Wang P, Jankovic J. The genetics of Parkinson disease. Ageing Research Reviews. 2018; 42: 72–85. https://doi.org/10.1016/j.arr.2017.12.007.

[5] Walter J, Bolognin S, Poovathingal SK, Magni S, Gérard D, Antony PMA, *et al*. The Parkinson's-disease-associated mutation LRRK2-G2019S alters dopaminergic differentiation dynamics via NR2F1. Cell Reports. 2021; 37: 109864. https://doi.org/10.1016/j.celrep.2021.109864.

[6] Croce JC, McClay DR. Evolution of the Wnt pathways. Methods in Molecular Biology (Clifton, N.J.). 2008; 469: 3–18. https://doi.org/10.1007/978-1-60327-469-2_1.

[7] Funayama M, Hasegawa K, Kowa H, Saito M, Tsuji S, Obata F. A new locus for Parkinson's disease (PARK8) maps to chromosome 12p11.2-q13.1. Annals of Neurology. 2002; 51: 296–301. https://doi.org/10.1002/ana.10113.

[8] Paisán-Ruíz C, Jain S, Evans EW, Gilks WP, Simón J, van der Brug M, *et al*. Cloning of the gene containing mutations that cause PARK8-linked Parkinson's disease. Neuron. 2004; 44: 595–600. https://doi.org/10.1016/j.neuron.2004.10.023.

[9] Zimprich A, Biskup S, Leitner P, Lichtner P, Farrer M, Lincoln S, *et al*. Mutations in LRRK2 cause autosomal-dominant parkinsonism with pleomorphic pathology. Neuron. 2004; 44: 601–607. https://doi.org/10.1016/j.neuron.2004.11.005.

[10] Orenstein SJ, Kuo SH, Tasset I, Arias E, Koga H, Fernandez-Carasa I, *et al*. Interplay of LRRK2 with chaperone-mediated autophagy. Nature Neuroscience. 2013; 16: 394–406. https://doi.org/10.1038/nn.3350.

[11] Migheli R, Del Giudice MG, Spissu Y, Sanna G, Xiong Y, Dawson TM, *et al*. LRRK2 affects vesicle trafficking, neurotransmitter extracellular level and membrane receptor localization. PloS One. 2013; 8: e77198. https://doi.org/10.1371/journal.pone.0077198.

[12] Juárez-Flores DL, González-Casacuberta I, Ezquerra M, Bañó M, Carmona-Pontaque F, Catalán-García M, *et al*. Exhaustion of mitochondrial and autophagic reserve may contribute to the development of LRRK2 ^{G2019S} -Parkinson's disease. Journal of Translational Medicine. 2018; 16: 160. https://doi.org/10.1186/s12967-018-1526-3.
[13] Nguyen HN, Byers B, Cord B, Shcheglovitov A, Byrne J, Gujar P, *et al*. LRRK2 mutant iPSC-derived DA neurons demonstrate increased susceptibility to oxidative stress. Cell Stem Cell. 2011; 8: 267–280. https://doi.org/10.1016/j.stem.2011.01.013.
[14] Kluss JH, Mamais A, Cookson MR. LRRK2 links genetic and sporadic Parkinson's disease. Biochemical Society Transactions. 2019; 47: 651–661. https://doi.org/10.1042/BST20180462.
[15] Wu YC, Sonninen TM, Peltonen S, Koistinaho J, Lehtonen Š. Blood-Brain Barrier and Neurodegenerative Diseases-Modeling with iPSC-Derived Brain Cells. International Journal of Molecular Sciences. 2021; 22: 7710. https://doi.org/10.3390/ijms22147710.
[16] Wang C, Xue Y, Markovic T, Li H, Wang S, Zhong Y, *et al*. Blood-brain-barrier-crossing lipid nanoparticles for mRNA delivery to the central nervous system. Nature Materials. 2025; 24: 1653-1663. https://doi.org/10.1038/s41563-024-02114-5.
[17] Jagaran K, Singh M. Lipid Nanoparticles: Promising Treatment Approach for Parkinson's Disease. International Journal of Molecular Sciences. 2022; 23: 9361. https://doi.org/10.3390/ijms23169361.
[18] Talwar P, Saha P, Mohan A, Divya S, Ravanan P. Drug delivery to the brain using endocytic receptors as carriers. In Neuroreceptor Endocytosis and Signaling in Health and Disease (pp. 435–456). Springer: Cham, Switzerland. 2025. https://doi.org/10.1007/978-3-031-81991-9_19.
[19] Yang F, Chen G. The nutritional functions of dietary sphingomyelin and its applications in food. Frontiers in Nutrition. 2022; 9: 1002574. https://doi.org/10.3389/fnut.2022.1002574.
[20] Jeon JH, Zhu H, Qin J, Wang L, Mou S, Langston LK, *et al*. Lipid Nanoparticles Formulated with a Novel Cholesterol-Tailed Ionizable Lipid Markedly Increase mRNA Delivery Both in vitro and in vivo. International Journal of Nanomedicine. 2025; 20: 9389–9405. https://doi.org/10.2147/IJN.S527822.
[21] Ahmad M, Saleem S, Ahmad AS, Yousuf S, Ansari MA, Khan MB, *et al*. Ginkgo biloba affords dose-dependent protection against 6-hydroxydopamine-induced parkinsonism in rats: neurobehavioural, neurochemical and immunohistochemical evidences. Journal of Neurochemistry. 2005; 93: 94–104. https://doi.org/10.1111/j.1471-4159.2005.03000.x.
[22] Jagaran K, Habib S, Singh M. Bio-Inspired Polymeric Solid Lipid Nanoparticles for siRNA Delivery: Cytotoxicity and Cellular Uptake In Vitro. Polymers. 2024; 16: 3265. https://doi.org/10.3390/polym16233265.
[23] Singh M. Assessing nucleic acid: Cationic nanoparticle interaction for gene delivery. In Narayanan K (ed.) Bio-Carrier Vectors (pp. 43–55). Springer: New York, NY, USA. 2021. https://doi.org/10.1007/978-1-0716-0943-9_4.
[24] Lugli E, Roederer M, Cossarizza A. Data analysis in flow cytometry: the future just started. Cytometry. Part a: the Journal of the International Society for Analytical Cytology. 2010; 77: 705–713. https://doi.org/10.1002/cyto.a.20901.
[25] Greggio E, Cookson M R, Savitt J M, Campbell K, Blackinton J, Farrer M J, *et al*. The Parkinson disease–associated leucine-rich repeat kinase 2 (LRRK2) is a dimer that undergoes intra molecular autophosphorylation. Journal of Biological Chemistry. 2008; 283:16906–16914. https://doi.org/10.1074/jbc.M708718200.
[26] Veiko AG, Sekowski S, Lapshina EA, Wilczewska AZ, Markiewicz KH, Zamaraeva M, *et al*. Flavonoids modulate liposomal membrane structure, regulate mitochondrial membrane permeability and prevent erythrocyte oxidative damage. Biochimica et Biophysica Acta. Biomembranes. 2020; 1862: 183442. https://doi.org/10.1016/j.bbamem.2020.183442.
[27] Gachowska M, Szlasa W, Saczko J, Kulbacka J. Neuroregulatory role of ginkgolides. Molecular Biology Reports. 2021; 48: 5689–5697. https://doi.org/10.1007/s11033-021-06535-2.
[28] Syahputra RA, Dalimunthe A, Utari ZD, Halim P, Sukarno MA, Zainalabidin S, *et al*. Nanotechnology and flavonoids: current research and future perspectives on cardiovascular health. Journal of Functional Foods. 2024; 120: 106355. https://doi.org/10.1016/j.jff.2024.106355.
[29] West AB, Moore DJ, Choi C, Andrabi SA, Li X, Dikeman D, *et al*. Parkinson's disease-associated mutations in LRRK2 link enhanced GTP-binding and kinase activities to neuronal toxicity. Human Molecular Genetics. 2007; 16: 223–232. https://doi.org/10.1093/hmg/ddl471.
[30] Cookson MR. The role of leucine-rich repeat kinase 2 (LRRK2) in Parkinson's disease. Nature Reviews. Neuroscience. 2010; 11: 791–797. https://doi.org/10.1038/nrn2935.
[31] Andreu Z, Yáñez-Mó M. Tetraspanins in extracellular vesicle formation and function. Frontiers in Immunology. 2014; 5: 442. https://doi.org/10.3389/fimmu.2014.00442.
[32] Chiasserini D, van Weering JRT, Piersma SR, Pham TV, Malekzadeh A, Teunissen CE, *et al*. Proteomic analysis of cerebrospinal fluid extracellular vesicles: a comprehensive dataset. Journal of Proteomics. 2014; 106: 191–204. https://doi.org/10.1016/j.jprot.2014.04.028.
[33] de Rus Jacquet A, Tancredi JL, Lemire AL, DeSantis MC, Li WP, O'Shea EK. The LRRK2 G2019S mutation alters astrocyte-to-neuron communication via extracellular vesicles and induces neuron atrophy in a human iPSC-derived model of Parkinson's disease. eLife. 2021; 10: e73062. https://doi.org/10.7554/eLife.73062.
[34] Lin CH, Tsai PI, Wu RM, Chien CT. LRRK2 G2019S mutation induces dendrite degeneration through mislocalization and phosphorylation of tau by recruiting autoactivated GSK3ß. The Journal of Neuroscience: the Official Journal of the Society for Neuroscience. 2010; 30: 13138–13149. https://doi.org/10.1523/JNEUROSCI.1737-10.2010.
[35] Smith JV, Luo Y. Studies on molecular mechanisms of Ginkgo biloba extract. Applied Microbiology and Biotechnology. 2004; 64: 465–472. https://doi.org/10.1007/s00253-003-1527-9.
[36] Xiong B, Lu JJ, Guo H, Huang M, Li T. Ginkgetin from Ginkgo biloba: mechanistic insights into anticancer efficacy. Natural Products and Bioprospecting. 2025; 15: 50. https://doi.org/10.1007/s13659-025-00535-6.
[37] Kim H, Kang S, Go GW. Exploring the multifaceted role of ginkgolides and bilobalide from *Ginkgo biloba* in mitigating metabolic disorders. Food Science and Biotechnology. 2024; 33: 2903–2917. https://doi.org/10.1007/s10068-024-01656-3.
[38] Guo N, Wang X, Xu M, Bai J, Yu H, Le Zhang. PI3K/AKT signaling pathway: Molecular mechanisms and therapeutic potential in depression. Pharmacological Research. 2024; 206: 107300. https://doi.org/10.1016/j.phrs.2024.107300.
[39] Ahlemeyer B, Krieglstein J. Neuroprotective effects of Ginkgo biloba extract. Cellular and Molecular Life Sciences: CMLS. 2003; 60: 1779–1792. https://doi.org/10.1007/s00018-003-3080-1.
[40] Nichols RJ, Dzamko N, Hutti JE, Cantley LC, Deak M, Moran J, *et al*. Substrate specificity and inhibitors of LRRK2, a protein kinase mutated in Parkinson's disease. The Biochemical Journal. 2009; 424: 47–60. https://doi.org/10.1042/BJ20091035.
[41] Kalita T, Dezfouli SA, Pandey LM, Uludag H. siRNA Functionalized Lipid Nanoparticles (LNPs) in Management of Diseases. Pharmaceutics. 2022; 14: 2520. https://doi.org/10.3390/pharmaceutics14112520.
[42] Bravo-San Pedro JM, Niso-Santano M, Gómez-Sánchez R,

Pizarro-Estrella E, Aiastui-Pujana A, Gorostidi A, *et al*. The LRRK2 G2019S mutant exacerbates basal autophagy through activation of the MEK/ERK pathway. Cellular and Molecular Life Sciences: CMLS. 2013; 70: 121–136. https://doi.org/10.1007/s00018-012-1061-y.

[43] Chen CY, Weng YH, Chien KY, Lin KJ, Yeh TH, Cheng YP, *et al*. (G2019S) LRRK2 activates MKK4-JNK pathway and causes degeneration of SN dopaminergic neurons in a transgenic mouse model of PD. Cell Death and Differentiation. 2012; 19: 1623–1633. https://doi.org/10.1038/cdd.2012.42.

[44] Henrich MT, Oertel WH, Surmeier DJ, Geibl FF. Mitochondrial dysfunction in Parkinson's disease - a key disease hallmark with therapeutic potential. Molecular Neurodegeneration. 2023; 18: 83. https://doi.org/10.1186/s13024-023-00676-7.

[45] Tanaka K, Galduróz RFS, Gobbi LTB, Galduróz JCF. Ginkgo biloba extract in an animal model of Parkinson's disease: a systematic review. Current Neuropharmacology. 2013; 11: 430–435. https://doi.org/10.2174/1570159X11311040006.

[46] Lejri I, Agapouda A, Grimm A, Eckert A. Mitochondria- and Oxidative Stress-Targeting Substances in Cognitive Decline-Related Disorders: From Molecular Mechanisms to Clinical Evidence. Oxidative Medicine and Cellular Longevity. 2019; 2019: 9695412. https://doi.org/10.1155/2019/9695412.

[47] Liu X, Hao W, Qin Y, Decker Y, Wang X, Burkart M, *et al*. Long-term treatment with Ginkgo biloba extract EGb 761 improves symptoms and pathology in a transgenic mouse model of Alzheimer's disease. Brain, Behavior, and Immunity. 2015; 46: 121–131. https://doi.org/10.1016/j.bbi.2015.01.011.

[48] Beal MF. Mitochondria take center stage in aging and neurodegeneration. Annals of Neurology. 2005; 58: 495–505. https://doi.org/10.1002/ana.20624.

[49] Wan W, Jin L, Wang Z, Wang L, Fei G, Ye F, *et al*. Iron Deposition Leads to Neuronal α-Synuclein Pathology by Inducing Autophagy Dysfunction. Frontiers in Neurology, 2017; 8: 1. https://doi.org/10.3389/fneur.2017.00001.

[50] Ravinther AI, Dewadas HD, Tong SR, Foo CN, Lin YE, Chien CT, *et al*. Molecular Pathways Involved in LRRK2-Linked Parkinson's Disease: A Systematic Review. International Journal of Molecular Sciences. 2022; 23: 11744. https://doi.org/10.3390/ijms231911744.

[51] van Attikum H, Gasser SM. Crosstalk between histone modifications during the DNA damage response. Trends in Cell Biology. 2009; 19: 207–217. https://doi.org/10.1016/j.tcb.2009.03.001.

[52] Osipov A, Chigasova A, Yashkina E, Ignatov M, Fedotov Y, Molodtsova D, *et al*. Residual Foci of DNA Damage Response Proteins in Relation to Cellular Senescence and Autophagy in X-Ray Irradiated Fibroblasts. Cells. 2023; 12: 1209. https://doi.org/10.3390/cells12081209.

[53] Hoeijmakers JH. Genome maintenance mechanisms for preventing cancer. Nature. 2001; 411: 366–374. https://doi.org/10.1038/35077232.

[54] Nicholls DG, Ferguson SJ. Bioenergetics. Academic Press: London, United Kingdom. 2013. https://doi.org/10.1016/C2010-0-64902-9.

[55] Di Maio R, Hoffman EK, Rocha EM, Keeney MT, Sanders LH, De Miranda BR, *et al*. LRRK2 activation in idiopathic Parkinson's disease. Science Translational Medicine. 2018; 10: eaar5429. https://doi.org/10.1126/scitranslmed.aar5429.

[56] Pal C. Targeting mitochondria with small molecules: A promising strategy for combating Parkinson's disease. Mitochondrion. 2024; 79: 101971. https://doi.org/10.1016/j.mito.2024.101971.

[57] Dhanya R, Kartha CC. Quercetin improves oxidative stress-induced pancreatic beta cell alterations via mTOR-signaling. Molecular and Cellular Biochemistry. 2021; 476: 3879–3887. https://doi.org/10.1007/s11010-021-04193-3.

[58] Dave A, Shukla F, Wala H, Pillai P. Mitochondrial Electron Transport Chain Complex Dysfunction in MeCP2 Knock-Down Astrocytes: Protective Effects of Quercetin Hydrate. Journal of Molecular Neuroscience: MN. 2019; 67: 16–27. https://doi.org/10.1007/s12031-018-1197-9.

[59] Lee MJ, Cho Y, Hwang Y, Jo Y, Kim YG, Lee SH, *et al*. Kaempferol Alleviates Mitochondrial Damage by Reducing Mitochondrial Reactive Oxygen Species Production in Lipopolysaccharide-Induced Prostate Organoids. Foods (Basel, Switzerland). 2023; 12: 3836. https://doi.org/10.3390/foods12203836.

[60] Chen M, Yan R, Luo J, Ning J, Zhou R, Ding L. The Role of PGC-1α-Mediated Mitochondrial Biogenesis in Neurons. Neurochemical Research. 2023; 48: 2595–2606. https://doi.org/10.1007/s11064-023-03934-8.